Research Paper

GEOSPHERE

GEOSPHERE, v. 15, no. 6

https://doi.org/10.1130/GES02139.1

14 figures; 1 table; 1 set of supplemental files

CORRESPONDENCE: gpiccion@ucsc.edu

CITATION: Piccione, G., Rasbury, E.T., Elliott, B.A., Kyle, J.R., Jaret, S.J., Acerbo, A.S., Lanzirotti, A., Northrup, P., Wooton, K., and Parrish, R.R., 2019, Vein fluorite U-Pb dating demonstrates post–6.2 Ma rare-earth element mobilization associated with Rio Grande rifting: Geosphere, v. 15, no. 6, p. 1958–1972, https://doi.org/10.1130/GES02139.1.

Science Editor: Andrea Hampel
Associate Editor: Christopher J. Spencer

Received 3 March 2019
Revision received 25 May 2019
Accepted 2 October 2019

Published online 8 November 2019

GOLD OPEN ACCESS

THE GEOLOGICAL SOCIETY OF AMERICA®

This paper is published under the terms of the CC-BY-NC license.

© 2019 The Authors

Vein fluorite U-Pb dating demonstrates post–6.2 Ma rare-earth element mobilization associated with Rio Grande rifting

Gavin Piccione[1,*], E. Troy Rasbury[1], Brent A. Elliott[2], J. Richard Kyle[2,3], Steven J. Jaret[1,4], Alvin S. Acerbo[5], Antonio Lanzirotti[5], Paul Northrup[1], Kathleen Wooton[1], and Randall R. Parrish[6]

[1]Department of Geosciences, Stony Brook University, Stony Brook, New York 11794, USA
[2]Bureau of Economic Geology, Jackson School of Geosciences, University of Texas at Austin, Austin, Texas 78713-8924, USA
[3]Department of Geological Sciences, Jackson School of Geosciences, University of Texas at Austin, Austin, Texas 78712-1101,USA
[4]Department of Earth and Planetary Sciences, American Museum of Natural History, New York, New York 10024, USA
[5]Center for Advanced Radiation Sources, Randall, Chicago, Illinois 60637, USA
[6]School of Earth and Environmental Sciences, University of Portsmouth, Portsmouth PO1 2UP, UK

ABSTRACT

Numerous studies have documented rare-earth element (REE) mobility in hydrothermal and metamorphic fluids, but the processes and timing of REE mobility are rarely well constrained. The Round Top laccolith in the Trans-Pecos magmatic province of west Texas, a REE ore prospect, has crosscutting fractures filled with fluorite and calcite along with a variety of unusual minerals. Most notably among these is an yttrium and heavy rare-earth element (YHREE) carbonate mineral, which is hypothesized to be lokkaite based on elemental analyses. While the Round Top laccolith is dated to 36.2 ± 0.6 Ma based on K/Ar in biotite, U-Pb fluorite and nacrite ages presented here clearly show the mineralization in these veins is younger than 6.2 ± 0.4 Ma (the age of the oldest fluorite). This discrepancy in dates suggests that fluids interacted with the laccolith to mobilize REE more than 30 m.y. after igneous emplacement. The timing of observed REE mobilization overlaps with Rio Grande rift extension, and we suggest that F-bearing fluids associated with extension may be responsible for initial mobilization. A later generation of fluids was able to dissolve fluorite, and we hypothesize this later history involved sulfuric acid. Synchrotron spectroscopy and laser ablation–inductively coupled plasma–mass spectrometry (LA-ICP-MS) U-Pb dating of minerals that record these fluids offer tremendous potential for a more fundamental understanding of processes that are important not only for REE but other ore deposits as well.

1. INTRODUCTION

Laser ablation–inductively coupled plasma–mass spectrometry (LA-ICP-MS) has revolutionized geochemical analyses because it significantly reduces measurement time and allows for sample exploration in the form of elemental maps and sample transects. LA-ICP-MS is especially useful for making trace-element measurements on rocks with heterogeneous compositions and complex fluid histories. The ability to preserve mineral fabrics is particularly important in geochronology, where spatiotemporal records aid geologic interpretations. For complex geologic systems, such as hydrothermally or metamorphically altered rocks, detail often occurs on scales smaller than even a <200 um laser can distinguish. In these cases, pairing LA-ICP-MS with spectroscopic techniques such as Raman or synchrotron is an innovative way to assess the geochemical composition of the rocks being analyzed.

Hydrothermally altered rocks often have complicated tectonic and fluid histories that make it difficult to reconstruct the processes leading to ore genesis in the rock record. Dating these geologically complex deposits remains challenging. Geochronologic methods, including K-Ar and Ar-Ar on K-bearing vein materials; Sm-Nd on fluorite and garnet; Rb-Sr on sphalerite; U-Pb and Th-Pb on calcite and several other less abundant U-bearing phases have added considerably to constraining ore mineralization. More recently, the application of in situ techniques such as laser ablation ICP-MS and sensitive high-resolution ion microprobe (SHRIMP) has greatly expanded the scope for dating mineralization, particularly with U-Pb dating of carbonates and opal (Li et al., 2004; Pfaff et al., 2009; Burisch et al., 2017; Tan et al., 2017; Yang et al., 2017; Walter et al., 2018).

We studied a suite of hydrothermal veins that crosscut the Round Top laccolith (referred to subsequently as Round Top) in the Trans-Pecos magmatic province of west Texas. These veins contain high concentrations of trace elements such as REE and U and are heterogeneous on a micro-scale. We used a variety of microscopy and spectroscopy techniques to elucidate the mineralogy and details of REE enrichment in this important REE deposit. Based on these findings, we used LA-ICP-MS U-Pb dating of fluorite, nacrite, and calcite to place age constraints on vein formation events. The combined approaches allow us to identify at least two types of fluids that show clear relationships to REE mobilization. Pairing absolute and relative geochronology with REE patterns, we identify multiple REE remobilization events that occurred between 6 and 4 Ma. Knowledge of the timing of geochemistry of these fluids might offer clues into the specific complexing ligands and the mechanism for remobilization.

*Current address: Earth and Planetary Sciences Department, University of California at Santa Cruz, California 95064, USA

Downloaded from https://pubs.geoscienceworld.org/gsa/geosphere/article-pdf/15/6/1958/4880292/1958.pdf
by Michael D. Campbell

Rare-earth elements have long been used as geochemical proxies to characterize hydrothermal environments. Fractionation of REEs in the fluid phase can be traced back to geochemical processes including sorption, complexation, and coprecipitation (Bau, 1991; Bau and Moller, 1992; Lottermoser, 1992). Remobilization of REE has been documented in several suites of hydrothermally altered rocks (Gieré, 1990; Ngwenya, 1994; Fan et al., 2004; van Dongen et al., 2010; Sheard et al., 2012; Genna et al., 2014; Li and Zhou, 2015; Debruyne et al., 2016; Cánovas et al., 2018). The mechanisms for REE remobilization are not well characterized (Williams-Jones et al., 2012; Li and Zhou, 2015). The use of geochronologic constraints to resolve REE remobilization paired with spectroscopic imaging techniques provides a possible framework for exploring these methods in future work.

2. GEOLOGIC SETTING

The Round Top Mountain rhyolite is part of the Sierra Blanca Complex, located within the Trans-Pecos magmatic province of west Texas (Fig. 1). The Trans-Pecos province extends to southern New Mexico to the north, the Pecos River to the east, and the Mexico-U.S. border to the west and south (Barker,1987; Henry and McDowell, 1986; Price et al., 1987, 1990; O'Neill et al., 2017). Trans-Pecos magmatism occurred mainly 48–32 Ma and has been divided into two major phases (Henry and McDowell, 1986; Henry et al., 1989; Price et al., 1990; Rubin et al., 1993). The early phase (48–38 Ma) is characterized by numerous small, silicic-to-mafic igneous intrusions, mafic lava flows, and two minor caldera eruptions (Henry and McDowell, 1986; Price et al., 1990). The late phase (38–32 Ma) is calc-alkalic and alkalic volcanism, comprising the most voluminous episode of Trans-Pecos magmatism (Henry and Price, 1984; Henry and McDowell, 1986; Price et al., 1990). Sierra Blanca Peak and, presumably, the rest of the Sierra Blanca Complex laccoliths, including Round Top, were emplaced during the main phase of Paleogene bimodal Trans-Pecos magmatic activity at 36.2 ± 0.6 Ma (K/Ar in biotite; Henry and McDowell 1986). Absolute ages of emplacement of the four other laccoliths have not been determined, but a relative emplacement sequence can be interpreted through major- and trace-element differentiation patterns. Based on the increasing enrichment of REEs, especially the increasing ratio of heavy REEs (HREEs) to light REEs (LREEs) between the five laccoliths, Triple Hill was emplaced first, followed sequentially by Sierra Blanca, Round Top, Little Sierra Blanca, and Little Round Top (Shannon, 1986; Shannon and Goodell, 1986; Price et al., 1990; Elliott, 2018). The small differences in highly evolved compositions and rapid cooling textures suggest the timing between emplacement and duration of emplacement was relatively short.

Round Top is one of only a few known minable REE resources in the United States. Previous work on the elemental composition of mineral grains by electron microprobe indicates that the REEs in the Round Top laccolith are hosted by bastnäsite-(Ce), (Ce)-rich fluorite, yttrofluorite, xenotime-Y, zircon, aeschynite-(Ce), a Ca-Th-Pb fluoride, and possibly ancylite-(La) and cerianite-(Ce) (Rubin et al., 1987; Price et al., 1990; O'Neill et al., 2017). Based on the anhedral and interstitial nature of the REE-bearing trace phases, they appear to crystallize late in the history of the laccolith (O'Neill et al., 2017). Additionally, synchrotron X-ray absorption fine structure spectroscopy (EXAFS) of the Round Top rhyolite has been used to suggest that virtually all the yttrium, a proxy for the chemical speciation of HREEs, is hosted in yttrofluorite (Bau and Dulski, 1995; Pingitore et al., 2014; Ponnurangam et al., 2015). Laccolith-hosted yttrofluorite is anhedral and interstitial in nature, suggesting that it crystallized late in the petrogenetic sequence. Yttrofluorite occurs along the outer portion of feldspar phenocrysts, within K-feldspar overgrowths, as inclusions, and within the K-feldspar portion of the rhyolite groundmass (O'Neill et al., 2017). Crosscutting fractures have mineral cements including fluorite and calcite.

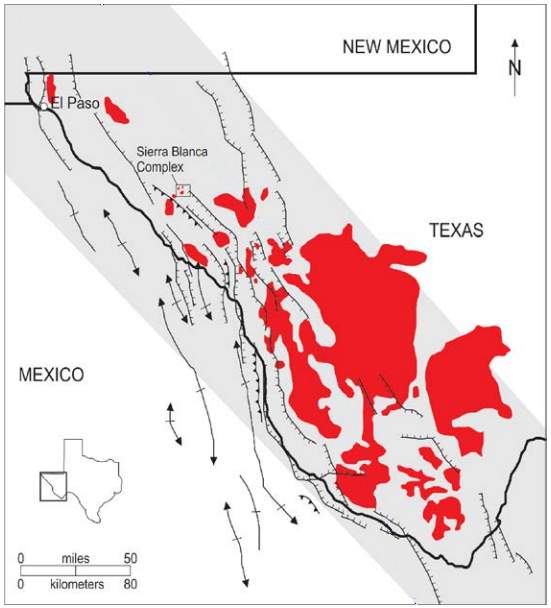

Figure 1. Location of the Sierra Blanca Complex (shown in red) relative to major geologic structures within the Trans-Pecos magmatic province. The gray shaded region represents the Texas lineament zone—a broad, ~80-km-wide zone of parallel transtensional faulting. Northwest-trending normal faults are related to Rio Grande rifting. Map modified from Muehlberger (1980), Price et al. (1990), and O'Neill et al. (2017).

Northwest-trending normal faults from Basin and Range extension dissect the Trans-Pecos region. Faults of similar orientation cut the Round Top laccolith (Fig. 1). Recent work on the Rio Grande rift suggests near synchronous rifting along the entire length between 25 and 10 m.y. ago (Ricketts et al., 2016). Based on basin subsidence, rifting was rapid until 8 Ma, followed by a significant hiatus coincident in time with Great Plains tilting at 6–4 Ma (van Wijk et al., 2018). It is suggested that the tilting and uplift are associated with a mantle

Downloaded from https://pubs.geoscienceworld.org/gsa/geosphere/article-pdf/15/6/1958/4880292/1958.pdf
by Michael D. Campbell

Data are reduced using latter software. No normalization is applied

Mineral type	La	Ce	Pr	Nd	Sm	Eu	Gd	Tb	Dy	Ho	Er	Tm	Yb	Lu
YHFE mineral	4.563	2.0969	17.4384	12.0979	16.4952	2.8804	37.7396	43.6392	151.0885	134.8528	149.9147	263.6688	288.6148	318.9375
YHFE mineral	0.0000	0.0000	0.0000	0.0000	0.0000	0.0000	0.0000	0.0000	0.0000	0.0000	0.0000	0.0000	0.0000	0.0000
YHFE mineral	20.39	1.538	61.3778	18.4887	45.4115	5.8306	79.4707	112.1851	230.1245	189.7657	357.7230	629.8424	663.2138	556.7555
YHFE mineral	26.0772	8.1186	30.0454	19.2122	72.9836	5.4897	112.3269	184.8397	286.8672	488.3571	886.9969	909.7361	1014.9398	598.1310
YHFE mineral	28.5005	5.4351	24.0154	2.4362	97.3208	6.8113	213.8973	181.7586	280.1824	313.4128	466.2764	327.1288	187.6494	164.5466
fluorite	0.0686	0.0357	0.1537	0.3088	0.3602	0.0416	0.7281	1.8174	3.1330	3.0087	4.9236	5.5452	5.6773	5.552
fluorite	0.0000	0.0000	0.0000	0.0000	0.0000	0.0000	0.0000	0.0000	0.0000	0.0000	0.0000	0.0000	0.0000	0.0000
fluorite	0.0282	0.0063	0.0728	0.0867	0.2678	0.018	0.2816	0.5885	0.8787	0.9877	1.1767	1.4644	1.138	1.2684
fluorite	0.0024	0.0004	0.0067	0.0091	0.2251	0.015	0.4302	1.877	1.9484	2.1792	2.5208	3.1929	3.3369	2.85
fluorite	0.0024	0.0014	0.0101	0.0119	0.0314	0.0052	0.0745	0.1206	0.2273	0.3425	0.4147	0.5035	0.5602	0.5115
fluorite	0.1548	0.0315	0.1547	0.3751	8.075	0.0823	1.8852	3.701	7.7397	6.0320	9.1057	11.0085	10.9562	8.4350
fluorite	0.0000	0.0000	0.0000	0.0000	0.0000	0.0000	0.0000	0.0000	0.0000	0.0000	0.0000	0.0000	0.0000	0.0000
fluorite	0.282	0.0508	0.5322	0.5359	1.1226	0.107	1.8348	1.4777	3.5286	6.0778	7.4767	8.0302	8.3001	7.8679
fluorite	0.0284	0.0084	0.084	0.0843	0.2008	0.0178	0.5111	0.7536	1.1034	1.3195	2.1138	2.4169	2.3904	2.168
fluorite	0.0448	0.0024	0.1165	0.2047	0.6724	0.0823	1.4852	2.1411	4.1021	4.4624	4.5328	5.3215	3.5841	2.7136
fluorite	0.1348	0.0014	0.3547	0.4019	8.968	0.07	1.4714	4.0386	6.6808	8.1471	10.4085	12.0819	12.2662	10.9618
fluorite	0.0000	0.0000	0.0000	0.0000	0.0000	0.0000	0.0000	0.0000	0.0000	0.0000	0.0000	0.0000	0.0000	0.0000
fluorite	0.0557	0.0007	0.068	0.0725	0.3403	0.0305	0.2815	0.5721	0.8978	1.1131	1.2358	1.3525	1.128	1.0544
fluorite	0.0171	0.0002	0.0162	0.0363	0.1389	0.0188	0.311	0.9399	1.7383	2.5851	3.5772	4.0363	4.3161	3.879
fluorite	0.0361	0.0005	0.1305	0.2412	0.5828	0.0502	0.9207	1.2871	3.0364	3.1285	3.5924	4.878	5.9108	3.102
fluorite	0.0192	0.0008	0.2358	0.2378	0.9855	0.0978	1.8995	2.2858	4.8243	3.9880	4.7885	5.5432	5.5649	4.38
fluorite	0.0000	0.0000	0.0000	0.0000	0.0000	0.0000	0.0000	0.0000	0.0000	0.0000	0.0000	0.0000	0.0000	0.0000
fluorite	0.0509	0.0059	0.3507	0.3935	0.8837	0.0895	0.7447	1.2364	2.7358	2.5385	3.6008	3.9024	3.9508	3.3092
fluorite	0.2289	0.0562	0.6897	0.5135	1.8348	0.1850	4.6355	12.2339	20.6204	23.7417	29.5187	37.184	28.8406	21.3137
fluorite	0.1358	0.0093	0.5517	0.9027	1.4819	0.1555	2.4550	6.1701	8.5882	13.5857	18.5884	20.1776	18.5923	14.8108
fluorite	0.1397	0.0015	0.7330	0.9378	2.5899	0.2468	5.1259	12.2401	21.1022	31.943	25.0987	26.4075	28.2235	18.4078
fluorite	0.0000	0.0000	0.0000	0.0000	0.0000	0.0000	0.0000	0.0000	0.0000	0.0000	0.0000	0.0000	0.0000	0.0000
fluorite	0.4364	0.0030	1.2413	1.3848	3.5768	0.3857	8.936	23.2484	40.5246	47.4848	58.5386	70.9568	68.4011	58.3598
fluorite	0.0425	0.0040	2.7586	2.6795	8.5708	0.8008	11.3145	25.8811	26.2844	45.584	52.0225	57.0457	53.1238	28.7557
fluorite	0.2388	0.0282	0.8376	0.8842	2.3838	0.2425	0.3025	0.7841	17.2481	20.2827	28.6125	30.5128	29.4021	18.7507
fluorite	0.6181	0.0158	2.3575	2.3571	5.6105	0.5267	10.3217	25.8811	42.0245	46.7027	58.1168	66.5188	66.4011	58.3598
fluorite	0.0000	0.0000	0.0000	0.0000	0.0000	0.0000	0.0000	0.0000	0.0000	0.0000	0.0000	0.0000	0.0000	0.0000
fluorite	0.1387	0.017	1.1033	1.2005	4.2774	0.4108	8.605	22.4266	36.2842	40.0257	52.0225	57.0457	58.781	58.3598
fluorite	0.0518	0.0058	0.3181	0.1567	0.9177	0.0313	0.5295	1.0882	1.8518	1.5245	1.628	1.583	1.694	1.2312
fluorite	0.0000	0.0000	0.0000	0.0000	0.0000	0.0000	0.0000	0.0000	0.0000	0.0000	0.0000	0.0000	0.0000	0.0000
fluorite	0.0282	0.0015	0.0728	0.0567	0.0159	0.0015	0.1014	0.2376	0.395	1.0969	2.4568	3.8778	3.9402	3.5128
fluorite	0.0028	0.0005	0.0865	0.0496	0.072	0.0109	0.2475	0.5846	1.1163	1.2893	2.4473	5.2125	5.7181	8.3079
fluorite	0.0148	0.008	0.0493	0.052	0.2172	0.0405	0.5227	0.7905	1.7181	2.5851	4.1276	8.2927	12.9482	12.9079
fluorite	0.0204	0.0141	0.1110	0.1125	0.3152	0.0112	0.844	2.2895	4.7795	8.3571	29.0987	37.1508	48.4728	47.8786
fluorite	0.0000	0.0000	0.0000	0.0000	0.0000	0.0000	0.0000	0.0000	0.0000	0.0000	0.0000	0.0000	0.0000	0.0000
fluorite	0.0058	0.0024	0.0278	0.0327	0.0199	0.0015	0.0154	0.2319	0.586	1.0968	4.5428	8.8778	9.9402	18.7508
fluorite	0.0426	0.0005	0.0865	0.0496	0.072	0.0109	0.2475	0.5846	1.1163	1.2893	2.4473	5.2125	5.7181	8.3079
fluorite	0.0148	0.008	0.0493	0.052	0.2172	0.0405	0.5227	0.7905	1.7181	2.5851	4.1276	8.2927	12.9482	12.9079
fluorite	0.0204	0.0141	0.1110	0.1125	0.3152	0.0112	0.844	2.2895	4.7795	8.3571	29.0987	37.1508	48.4728	47.8786
fluorite	0.0058	0.0024	0.0227	0.0327	0.0199	0.0144	0.0464	1.441	2.6284	3.1125	16.1854	27.5171	48.4648	16.5085

[1]Supplemental Materials. Supporting Materials 1: Outcrop photos. Data Set S1: U-Th-Pb raw data with data reduction math. Data Set S2: REE data for each mineral analyzed. Data Set S3: Metadata associated with data acquisition, processing, and reporting following Horstwood et al. (2016). Data Set S4: Compilation of WC-1 standard analyses associated with each unknown analyte. Table S1: Compilation of ages organized by sample. Please visit https://doi.org/10.1130/GES02139.S1 or access the full-text article on www.gsapubs.org to view the Supplemental Materials.

upwelling and the rate of extension has remained similar since this tilting (van Wijk et al., 2018). A compilation of strain rates across the western United States shows extension in the region beginning ca. 20 Ma and continuing to the present with important transtension between 12 and 4 Ma (Bahadori et al., 2018). Melt inclusions in olivine from basalts of the Rio Grande rift show an east to west decrease in volatiles particularly in the southern Rio Grande rift (Rowe et al., 2015). Changes in volatile budgets through time appear to reflect increasingly important asthenosphere sources following the loss of the Precambrian lithosphere (Rowe et al., 2015).

3. ANALYTICAL METHODS

We collected samples from an ~10-m-wide highly brecciated zone within one of these fault zones (pictured in Supporting Materials 1[1]). Samples were taken from within a mineralized zone that had a variety of textures with evidence for brecciation and dissolution followed by new generations of mineral formation. The vein material was found within a powdery, disaggregated matrix, and the orientations of the vein materials were not likely primary.

3.1 Sample Preparation

Samples were slabbed and polished into approximately cm-sized, mm-thick wafers for scanning electron microscopy (SEM), synchrotron X-ray spectromicroscopy, Raman spectroscopy, and laser ablation analyses.

3.2 Elemental Microscopy

Scanning electron microscopy imaging and element dispersive spectra (EDS) analyses were performed at Stony Brook University (SBU) Material Sciences facility with a Zeiss LEO1550 SEM. Samples were gold coated twice with 3 nm (6 nm total) at an angle of 30° using an Edwards 150B "sputter coater." Samples were mounted together, and copper tape was placed across samples to prevent charging of the surface. Images were collected with a Robinson backscatter detector (RBSD) and a beam energy of 20 keV. The EDS and EDAX spectra were collected from an EDAX Phoenix sapphire detector, using software and electronics from iXRF Systems.

3.3 Raman Spectroscopy

Micro-Raman spectroscopy was conducted at the Center for Planetary Exploration (CPEX) at SBU. We used a WITec alpha300 R confocal imaging system equipped with 532 nm Nd:YAG (neodymium-doped yttrium aluminum garnet; Nd:$Y_3Al_5O_{12}$) laser with 5 mW nominal power at the sample surface and a 50× (NA = 0.8) objective (spot size of 763 nm). Spot analyses consisted of 240 1-second integrations, which were averaged. Micro-Raman maps consist of 75 × 75 µm areas acquired with 150 × 150 points per line and integration times of 0.3 seconds. Removal of cosmic rays and visualization were done within the WITec Control4 software.

3.4 Synchrotron XRF Spectromicroscopy

Initial micro-focused synchrotron X-ray fluorescence (S-XRF) imaging was performed at the X-ray microprobe beamline X26A, at the National Synchrotron Light Source (NSLS), Brookhaven National Laboratory. Mapping was conducted using a monochromatic X-ray beam tuned to 18 keV using a Si(111) channel-cut monochromator. Monochromatic X-rays were focused to a beam size of 5 × 8 µm (V × H) using a pair of 100-mm-long, elliptically bent, Rh-coated silicon mirrors in a Kirkpatrick-Baez geometry. Photon flux at this incident beam energy was ~3 × 10^9 photons per second. X-ray fluorescence spectra were collected using two single-element Vortex-EX silicon-drift-diode detectors and one four-element Vortex-ME4 silicon-drift-diode detector (SII Nanotechnology). Compositional maps were collected in a continuous scan mode as described in Lanzirotti et al. (2010).

Follow-up synchrotron XRF elemental imaging was performed at the submicron-resolution X-ray spectroscopy (SRX) and X-ray fluorescence microprobe (XFM) beamlines at the National Synchrotron Light Source II (NSLS-II), as well as the beamline 13-ID-E at the advanced photon source (APS). At the SRX beamline, samples were mounted at 35° to incident beam, while a three-element silicon-drift-diode detector was placed at 90° relative to the incident beam. XRF maps were collected by raster scanning samples through the micro-focused beam with a spot size of 2 × 2 µm. At the X-ray fluorescence microprobe (XFM) beamline, a large XRF map was collected with the sample mounted at 45° relative to the micro-focused incident beam with a spot size of 5 × 8 µm. Data were collected using on-the-fly scanning with a 125 ms dwell time using a four-element Vortex-ME4 silicon-drift-diode detector with incident energy tuned to 17.3 keV. At beamline 13-ID-E, samples were mounted at 45° relative to the incident beam, and samples were raster scanned with a micro-focused spot size of 1 × 1 µm. X-ray fluorescence was measured with an incident beam energy to two different energies above and below the U L-edge binding energy, 17.08 and 17.18 keV, using a four-element silicon-drift-diode detector (Hitachi) mounted at 90° relative to incident beam. Two incident beam energies, 17.08 and 17.18 keV, above and below the U L-edge binding energy, were used at 13-IDE to correct for spectral overlaps of the U L-edge emission lines with emission lines due to Rb and Sr K-edge fluorescence, which in fluorite can be very pronounced with energy dispersive analysis at the energy resolution of the detector. These overlaps are strongest on the U Lα emission line but negligible when generating maps using the U Lι.

S-XRF microprobe measurements were made in the "tender" energy range of 1 to 5 keV, at the tender energy X-ray spectroscopy (TES) beamline 8-BM and at NSLS-II and at beamline X15B at NSLS (Northrup et al., 2016; Northrup,

Downloaded from https://pubs.geoscienceworld.org/gsa/geosphere/article-pdf/15/6/1958/4880292/1958.pdf
by Michael D. Campbell

2019). Incident beam energy was set to 3555 eV with Si (111) monochromator crystals and focused to a 5 × 10 μm spot size for large elemental maps and for microbeam X-ray absorption spectroscopy and was reduced to 2 × 3 μm for fine mapping. Earlier measurements at X15B (NSLS precursor to TES) used a spot size of 10 × 15 μm and Si (111) monochromator. Samples were oriented at 45° to beam, and fluorescence was measured using a Canberra ultra-low–energy Ge detector. Setting an energy of 3555 eV stimulates fluorescence from the U M_5 edge, the Y L_3 edge, and the S, Si, Al, and Mg K-edges but is below the Ca K-edge to avoid interferences from that major element. Energy scanning was conducted in quick on-the-fly mode, 10–30 seconds per scan with multiple scans at selected pixels of the elemental maps.

3.5 Laser Ablation Element Analyses and U-Pb Geochronology

Laser ablation–inductively coupled plasma–mass spectrometry (LA-ICP-MS) analyses were conducted at the Facility for Isotope Research and Student Training (FIRST) at SBU. A 213 UV New Wave laser system coupled to an Agilent 7500cx quadrupole ICP-MS was used for the analyses. Data sets include ^{238}U, ^{232}Th, ^{208}Pb, ^{207}Pb, and ^{206}Pb isotopes, which were collected sequentially for 0.1 seconds each throughout 30 second ablations. An 80 μm spot size was used for most of the analyses (40 and 160 μm spots were also used in some of the sequences). For all of the analytical sessions, unknowns were bracketed by at least five standard spots, and two standard spots were interspersed after every five unknown spots. A typical session includes 20–30 unknowns and 16–20 standards. The WC-1 calcite standard (Roberts et al., 2017) was used as a standard of known age for all mineralogies (carbonate, fluorite, and other minerals) due to the lack of standards for these unusual minerals, and National Institute of Standards and Technology (NIST) 612 was used for Pb isotope fractionation correction and for approximating element concentrations using signal intensity ratios. Data were reduced in iolite (Paton et al., 2011) using the U-Pb Geochronology 3 (or 4) data reduction scheme for U-Pb analyses with NIST 612 as the primary Pb-U standard. Element concentrations were processed with the trace-element data reduction schemes (DRS) in semiquantitative mode using NIST 612 as the standard. These DRS subtract baselines and correct for downhole fractionation and drift of the signal.

For U-Pb LA-ICP-MS, reduced data are plotted using Isoplot (Ludwig, 1998, 2003, 2012) on a modified Tera-Wasserburg isochron plot following the procedure of Parrish et al. (2018). This method calculates radiogenic ^{208}Pb from ^{232}Th decay and then subtracts it from total ^{208}Pb to find the amount of common ^{208}Pb (208c). This value is then used in plotting ^{208}Pb/^{206}Pb versus ^{238}U/^{206}Pb. Using ^{208}Pbc/^{206}Pb also allows for common Pb-corrected ^{238}U/^{206}Pb ages without having to measure ^{204}Pb. Using this plot, the age and uncertainty corresponding to the X-axis intercept were used. Individual data points were also corrected for common Pb using a Stacey-Kramers model age value of ^{208}Pb/^{206}Pb and plotted as a weighted average for related samples (Data Set S1 [footnote 1]). All uncertainties on age calculations were reported as 2σ.

A secondary normalization used WC-1 for calcite, fluorite, and nacrite. Although it would have been desirable to have matrix-matched standards, we make the assumption that while some bias between calcite and fluorite may exist, it is likely to be less than the ~7% demonstrated by Parrish et al. (2018) between calcite and zircon. A further potential issue in our dating is the lack of knowledge of the initial U activity ratio (^{234}U/^{238}U) of the U-rich fluids. High activity can lead to the presence of unsupported ^{206}Pb, which would cause age calculations to be too old. This effect has been well documented in calcite in speleothems of later Pleistocene age. However, given the mainly late Miocene and Pliocene ages of this study, it would be nearly impossible to measure any residual disequilibrium, and therefore we are unable to make any quantifiable correction for this effect. We have not added any additional uncertainty arising from these sources of potential bias because they are likely insignificant relative to the range of ages and magnitude of reported uncertainties presented here and therefore hold little potential to change the overall interpretation of ages and their geological significance. Furthermore, isochron ages presented here have a spread of mean square of weighted deviates (MSWDs) that range from under to over dispersed, with some much larger than 1. Modeled ages with over-dispersed MSWDs are treated with caution, but the ages are entirely consistent with better constrained isochrons.

4. RESULTS

4.1 Host Rhyolite Relationships to Vein Minerals within the Fracture Zone

Within the fracture zone, we find fragments of host rhyolite with and without vein minerals. Veins that cut the host rock (Figs. 2A and 2B) are filled with a mixture of nacrite and fluorite. Fragments of host rock and nacrite show in situ brecciation, and the area around the breccia clasts is filled by a white calcite cement (Figs. 2B–2D and 2G). Nacrite, which can be light purple (Figs. 2B and 2D top), pink (Fig. 2G), light green (Fig. 2D bottom), or tan (Fig. 2C), commonly forms layers that are followed by green fluorite and then white calcite (Figs. 2B–2D). As seen in Figure 2D, sometimes these layers appear to have formed on a preexisting calcite cement. A YHREE carbonate, which we hypothesize to be lokkaite but refer to henceforth as YHREE carbonate due to uncertainty in its identification, commonly occurs at boundaries between fluorite and calcite, as shown in section 4.1.3. Fluorite is also found alone (Fig. 2E) as well as in the form of brecciated clasts within white calcite matrix (Fig. 2F and 2G). Some examples of the breccia have clasts of primarily nacrite and fluorite within a white calcite cement (Fig. 2G). Calcite is the principal mineral within the fracture with a variety of geometries and types, but the most common of those is a lighter-colored calcite. Dark-brown calcite occurs both as a mixture and independent of this white calcite (Fig. 2H). There are variations on the samples shown here with fluorite and nacrite forming layers as well as clasts. We have not found calcite as clasts in the breccia. We see a

Downloaded from https://pubs.geoscienceworld.org/gsa/geosphere/article-pdf/15/6/1958/4880292/1958.pdf
by Michael D. Campbell

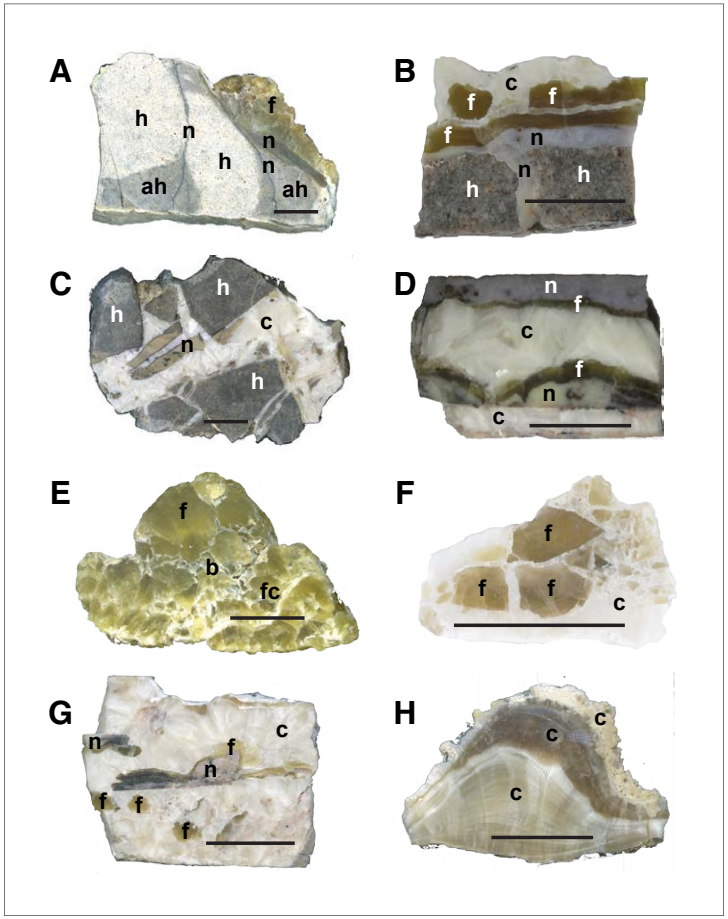

Figure 2. Visible light images of the samples from the fracture. (A) Host rock with small veins that are filled by nacrite and capped by fluorite. (B) Fractured host rhyolite with nacrite between fragments and on surfaces followed by fluorite, which is brecciated and cemented by calcite. (C) Brecciated host rhyolite and nacrite that is cemented by calcite. (D) Layered vein material with the calcite on the bottom appearing to be the surface upon which nacrite followed by fluorite followed by calcite grew. These minerals appear to come from the top and bottom. (E) Brecciated green fluorite with calcite filling between some fragments. (F) Brecciated fluorite with calcite cement. (G) Breccia with nacrite and fluorite clasts. (H) Two generations of calcite. The white to amber calcite is highly enriched in rare-earth elements (REEs). The brown calcite is low in REE but has high U-Pb ratios. Labels are: h—host; ah—altered host; n—nacrite; f—fluorite; fc—fluorite with calcite; c—calcite; b—brecciated zone. Not visible here is the yttrium and heavy rare-earth element (YHREE) carbonate that lines the breccia clasts and occurs between fluorite and calcite. Scale bars are all 1 cm.

gradation between layered samples (Figs. 2B and 2D) and highly brecciated samples (Figs. 2C, 2F, and 2G). Calcite appears to mineralize last, filling spaces and perhaps displacing other minerals during growth in at least some cases. For example, in Figure 2B, the green fluorite is fragmented and separated by calcite even though it forms a layer over nacrite.

4.1.1 Nacrite

Raman mapping of the microcrystalline phase shown in Figures 2B, 2D, and 2G (labeled n) is consistent with nacrite $Al_2Si_2O_5(OH)_4$ with several strong Raman peaks at 126, 195, 318, 524, 747, 3619, and 3696 Δ cm^{-1} (Figs. 3B and 3C). Raman maps are consistent elemental chemistry, which indicates an Al-rich phase. In some cases, other cations (particularly Mg and Fe) are present, which may indicate a solid solution with dickite. Raman spectroscopy is not able to distinguish between nacrite and dickite. Here, for simplicity, we refer to this phase as nacrite, although we note there may be chemical complexity. The peak at 318 Δ cm^{-1} is consistent with fluorite, suggesting that this phase is a mix of nacrite + fluorite (Fig. 3C). This nacrite and fluorite association is at the submicron scale, because it is not possible to distinguish between them at the highest magnification with the SEM or mapping with a Raman spot size

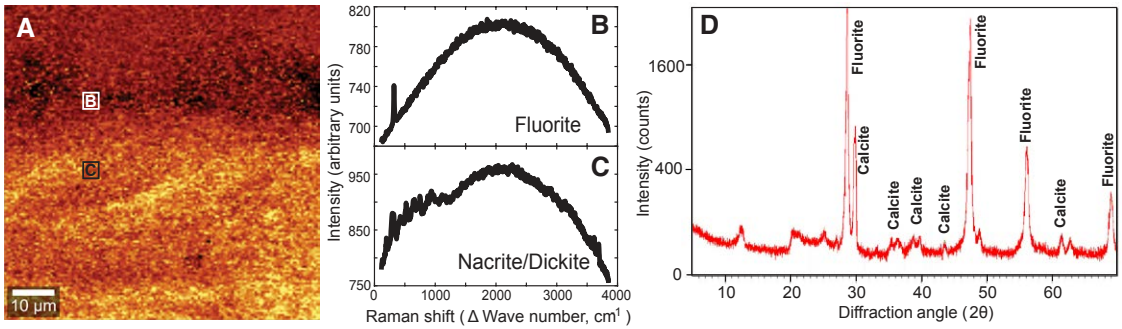

Figure 3. (A) Raman map of vein material. Dark region on top is fluorite (spectra shown in B); lighter region on the bottom is nacrite (spectra shown in C). (B) Raman spectra indicate fluorite. (C) Raman spectra from cryptocrystalline phase show the presence of nacrite. (D) X-ray diffraction (XRD) spectra of a selected cryptocrystalline phase indicate mixture of fluorite, calcite, and a weakly crystalline phase(s) consistent with nacrite.

Downloaded from https://pubs.geoscienceworld.org/gsa/geosphere/article-pdf/15/6/1958/4880292/1958.pdf
by Michael D. Campbell

of 763 nm (Fig. 3C), but XRD confirms the presence of fluorite in this phase (Fig. 3D; Table 1). Nacrite is found as layers and crosscutting veins within the host rhyolite and as breccia clasts within white calcite matrix. Based on crosscutting relationships between nacrite and the host rock, as well as nacrite's relationship with fluorite and calcite, nacrite appears to be the first mineral deposited in the fracture zone. Nacrite is always associated with fluorite in these veins, both as an intimate mix and with fluorite capping it.

No finely dispersed REE phases are identifiable in the nacrite using SEM imaging. Synchrotron XRF element mapping shows areas of elevated concentrations of Y within nacrite, suggesting that it is either itself Y enriched or that it contains finely dispersed REE minerals at less than the spatial resolution of the incident beam (2 µm, Fig. 4B). Yttrium X-ray absorption near edge structure (XANES) spectra collected for enriched areas in the nacrite are indistinguishable from spectra collected from YHREE carbonate, while dissimilar from spectra collected from the host rock (Fig. 4A). It thus is likely that Y is present as a similar chemical species in both materials.

Nacrite (dickite) co-occurs with the YHREE carbonate where it lines a zone of brecciation and dissolution within fluorite (Fig. 5D). While nacrite has an intimate association with fluorite in the examples described above, this example shows it can also coexist with the YHREE carbonate independent of fluorite. The mineral is too small to be analyzed by XRD, but Raman spectroscopy confirms it is either nacrite or dickite. Scanning electron microscopy EDS analyses (and TES XRF imaging) demonstrate that some (but not all) occurrences of this mineral have Mg (Figs. 5D and 5G), suggesting it is dickite. Based on microstratigraphic relationships, the clay mineral that occurs with the YHREE carbonate forms later than the green fluorite it caps.

TABLE 1. X-RAY DIFFRACTION (XRD) OF Al-Si PHASES

Sample	Fluorite (%)	Nacrite (%)	Mg-calcite (%)
Tan mineral shown in Figure 2C	70.3 (1.4)	13.3 (0.7)	16.4 (0.7)
Purple mineral shown in Figure 2D	83.6 (2.2)	16.4 (2.6)	Not detected
White mineral shown in Figure 2E	91.5 (6.1)	8.5 (6.4)	Not detected

Notes: Data were collected for two hours on a spinning stage; data were processed in X'pert Highscore Plus software; numbers are calculated percent of total as determined by spectral fitting.

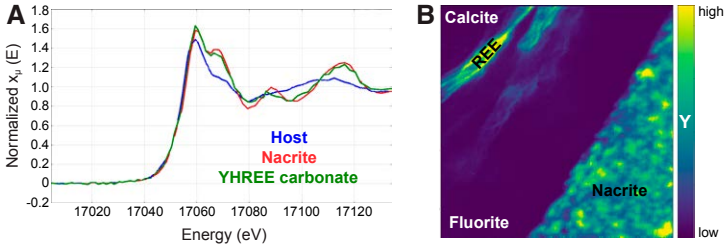

Figure 4. (A) Yttrium K-edge X-ray absorption near edge structure (XANES) (YHREE carbonate mineral—green; nacrite—red; host rock—blue). Data from submicron-resolution X-ray spectroscopy (SRX) at the National Synchrotron Light Source (NSLS) II. (B) Synchrotron X-ray fluorescence (S-XRF) map (blue—low concentration; yellow—high concentration) showing Y-rich mineral lining fluorite (rare-earth element) and Y-rich spots in the nacrite. Map dimensions are 0.2 × 0.2 mm. YHREE—yttrium heavy rare-earth element.

4.1.2 Green Fluorite

Green fluorite is a common phase within the fracture zone. It is found capping the host (Fig. 2A), as layers following nacrite (Figs. 2B and 2D), as clasts within calcite-cemented breccia (Figs. 2F and 2G), and predominantly as fluorite that can be brecciated and have calcite veins (Fig. 2E). Synchrotron XRF element mapping reveals that there are (at least) two distinct generations of similar color fluorite that are separated by a brecciated zone (Figs. 2 and 6). One generation (the top part of Figs. 2E and 6) is enriched in Sr and lower in U; the other generation (the bottom part of Figs. 2E and 6) is enriched in U and lower in Sr. The U in fluorite was determined to be in the 6+ oxidation state by U M_5-edge and L_3-edge XANES. Scanning electron microscopy element mapping reveals fragments of fluorite in the brecciated zone with evidence of dissolution (Fig. 5D). Within the brecciated zone, void surfaces (the voids are easily visualized by examining the Ca map in Fig. 6) are coated with an YHREE mineral, as shown by the Y map (Fig. 6). Physically, the two generations are distinct because the top part is clear, without obvious inclusions, while the bottom part has opaque white layers (Fig. 2E). The white layers are calcite and are discussed below in section 4.1.4.

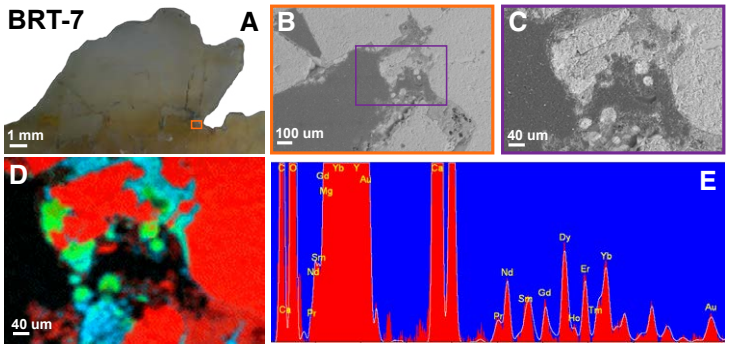

Figure 5. (A) Visible light image of brecciated green fluorite. (B) Scanning electron microscopy (SEM) image from the orange boxed area on A. (C) Further zoom on the brecciated fluorite; area indicated by the purple box in B. (D) RGB color image of area in C; red—Ca (fluorite); blue—Mg (dickite and nacrite); green—Y (YHREE-bearing carbonate). (E) Energy-dispersive X-ray (EDX) spectra of yttrium and heavy rare-earth element (YHREE) carbonate mineral. Note resorbed texture in the fluorite and the close spatial association of the YHREE mineral and dickite.

Downloaded from https://pubs.geoscienceworld.org/gsa/geosphere/article-pdf/15/6/1958/4880292/1958.pdf
by Michael D. Campbell

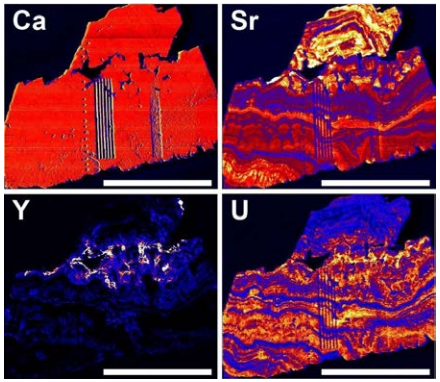

Figure 6. Synchrotron X-ray fluorescence (S-XRF) maps from X26A, National Synchrotron Light Source (NSLS). White bar is 1 cm. Lines and spots on surface are from laser ablation. Ca—calcium; Sr—strontium; Y—yttrium; and U—uranium.

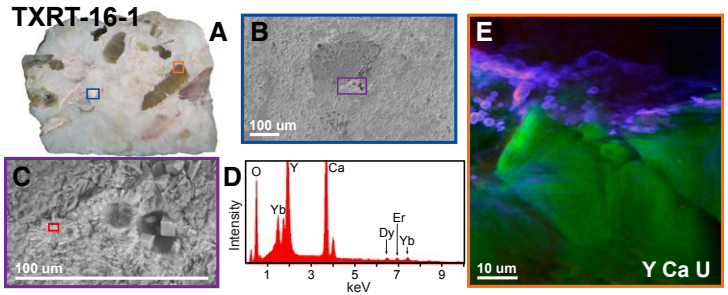

Figure 7. (A) Visible light image of vein breccia. (B) Scanning electron microscopy (SEM) image of area in blue box on A. (C) SEM image of area in purple box on B; shows nodules of yttrium and heavy rare-earth element (YHREE) mineral. (D) Energy-dispersive X-ray (EDX) spectra from area outlined by red box in C. (E) Synchrotron X-ray florescence (S-XRF) elemental image taken at 13-ID-E beamline of the edge of a fluorite clast; area of image outlined by orange box in A. RGB coloration is Y, Ca, and U, respectively.

4.1.3 YHREE Carbonate

A YHREE carbonate is found coating dissolution surfaces and lining breccia clasts. This mineral is sometimes associated with nacrite and dickite (Fig. 5D) and is often followed by calcite. A zone of brecciation and dissolution in the green fluorite provides important insight into the timing of this YHREE carbonate, precipitating after green fluorite, directly on dissolution surfaces (Figs. 5D and 6Y).

Similarly, clasts of nacrite and fluorite in breccia samples (such as shown in Figs. 2F and 2G) are coated by an YHREE carbonate mineral that is followed by white calcite (Fig. 7). Energy dispersive spectra mapping of Y shows the pervasive nature of the YHREE mineral coating clasts as well as other surfaces (Figs. 6Y and 7B–7E). The YHREE carbonate is also arranged in nodules (Fig. 7C). Based on EDS spectra, the REE mineral contains Ca, Y, C, O, and HREEs (Fig. 7D) and is most likely lokkaite [$Ca(Y,Gd,Nd,Dy)_4(CO_3)_7 \cdot 9H_2O$].

4.1.4 Calcite

Calcite from within the vein appears to be the latest phase, with multiple generations that may be separated by dissolution surfaces shown by the irregular contacts between generations. Many calcite samples are tabular, suggesting that they formed along fracture surfaces. Most samples have unfilled pore space between layers, suggesting calcite growth does not displace existing vein minerals or that dissolution followed growth. The layers typically show a pattern of growth that alternates between white and brown (Figs. 8A–8C). When viewed in plan view, brown calcite appears to form elongated cm-wavelength ridges on the surface (Fig. 8A). These ridges are underlain by mounded brown calcite (Fig. 8A), suggesting its formation and possibly dissolution are responsible for the ridges. The brown calcite is capped by a spongy tan calcite that appears to be a residue (Fig. 8A). When polished, the white calcite appears to be more amber with white layers (Figs. 8B and 8C). These white layers have elevated Y (Fig. 8C), while the overlying brown calcite has low Y and high U (Fig. 8C).

With SEM imaging, we observed the YHREE carbonate on the irregular surface at the base of the white calcite shown in Figure 8. Synchrotron XRF maps show the REE coating the calcite surface (Fig. 8D). The REE and Y are also elevated in the white layers of the calcite as shown by LA element maps (Fig. 8C). Synchrotron XRF maps show that some REEs occur as discrete phases within the calcite (Fig. 8E). The S-XRF element map also reveals the brecciated nature of the REE-enriched contact between white and brown calcite (Fig. 8E).

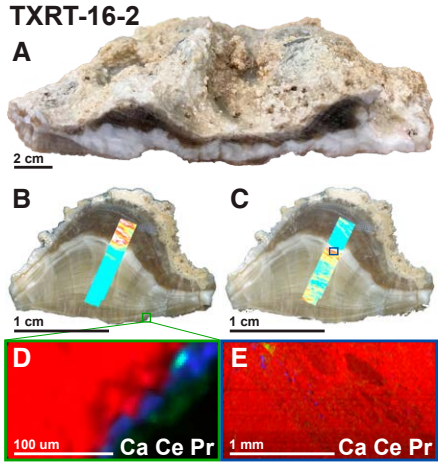

Figure 8. (A) Visible light photo of vein as shown in Figure 2H. (B) Cross section of slab cut from sample in A. Laser ablation map of U concentration (hot colors = high; cold colors = low). (C) Cross section of slab cut from sample in A. Laser ablation map of yttrium (Y) concentration (hot colors = high; low colors = low). (D, E) Composite RGB X-ray fluorescence (XRF) elemental maps taken at submicron-resolution X-ray spectroscopy (SRX); area corresponding to green and purple boxes in B and C, respectively. RGB maps are Ca, Ce, and Pr, respectively.

Downloaded from https://pubs.geoscienceworld.org/gsa/geosphere/article-pdf/15/6/1958/4880292/1958.pdf
by Michael D. Campbell

Scanning electron microscopy imaging and S-XRF mapping with TES reveal that the opaque white layers within the brecciated fluorite sample (Fig. 2E) are calcite filling dissolution voids after fluorite (Figs. 9B and 9C). Silicon, S, and Y line dissolution surfaces (Figs. 9C and 9D), and Si and Y are highly correlated (Fig. 9D). Uranium is highly concentrated in fluorite, and the U maps show cubic shapes that are now skeletal that are associated with S (Figs. 8E and 9E). Element dispersive spectra of the calcite, at high magnification, without evidence for other phases, show that Al and Si are present at this scale (Fig. 9F).

4.1.5 Mineral Relationships and REE Patterns

We studied a sample that contains all of the recognized phases described above to illuminate mineral relationships (Fig. 10). We used S-XRF mapping at hard (Fig. 10B) and tender energy (Fig. 10C) ranges to map Ca, Al, Mg, S, Si, Y, U, and Fe in this sample. Al and Mg clearly delineate nacrite (Fig. 10B). By comparison, it is clear that S, Ca, Sr, Y, and U are elevated in nacrite (Figs. 10B and 10C). Uranium is highly elevated but zoned in fluorite (Figs. 10B and 10C). The YHREE mineral, as illustrated by the map pattern of Y, occurs between calcite and nacrite (Figs. 10B and 10C), and between fluorite and calcite (Figs. 9D and 9E), but not between nacrite and fluorite.

Rare-earth element patterns based on element analyses by LA-ICPMS show differences between phases. The REE patterns for the nacrite show pronounced negative Ce and Eu anomalies, with middle and heavy REE enrichment and a hump in the MREE (Fig. 11A). Green fluorite has lower REE concentrations but a very similar pattern to the nacrite (Fig. 11B). Calcite also shows the pronounced negative Ce and Eu anomalies, but it is far more depleted in the LREEs and shows a steep rise to the HREE, quite distinct from the nacrite and fluorite REE patterns (Fig. 11C). In some calcite samples, there is a slight increase to higher enrichment in the REE heavier than Ho, perhaps due to mixing with the YHREE mineral (Fig. 11C). Rare-earth element patterns obtained on brown calcite show similar patterns with pronounced negative Ce and Eu anomalies and HREE enrichment. Calcite crust does not have particularly elevated REE, although it does show the typical HREE enrichment of calcite. The YHREE carbonate has middle to heavy REE patterns with a hump at Er (Fig. 11D). Some of the REE elevated areas are more enriched in the light REE.

4.2 U-Pb Geochronology

Fluorite, nacrite, and brown calcite within Round Top fractures are enriched in U and have favorable U-Pb ratios. There are multiple generations of all of these phases based on their relative order as well as on the differences in color, geochemistry, and ages. Traditional Tera-Wasserburg plots yield analytically indistinguishable ages to modified Tera-Wasserburg plots using ^{232}Th-corrected ^{208}Pb as the normalizing isotope. Thus, we follow Parrish et al. (2018) and use the 86TW plot and common Pb-corrected, weighted-average ^{238}U-^{206}Pb plots.

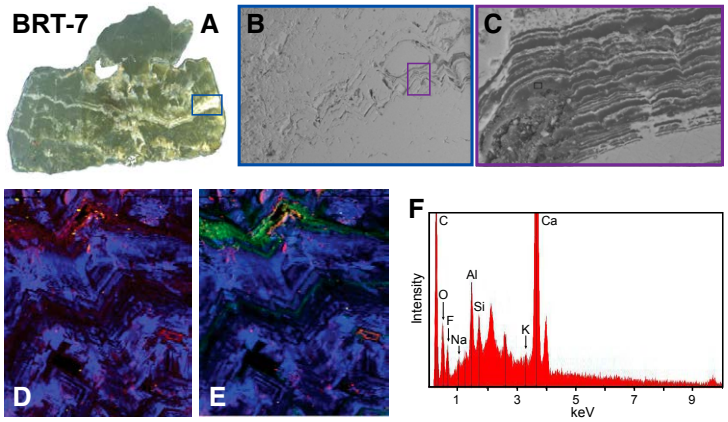

Figure 9. (A) Visible light image of brecciated green fluorite sample as shown in Figure 3E. (B) Scanning electron microscopy (SEM) image from inset area outlined in blue box in A. (C) SEM image of area outlined in purple box in B. (D) X15B RGB map of Y, Si, U, respectively. (E) X15B RGB map of Y, S, and U, respectively. (F) Energy-dispersive X-ray (EDX) spectra of calcite show that Al and Si are present even at high magnification.

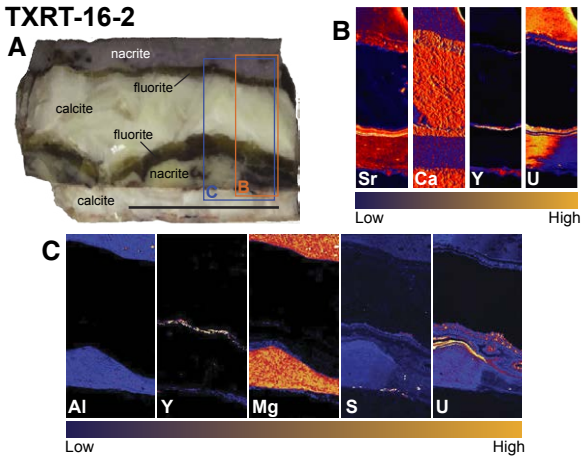

Figure 10. (A) Visible light image of a layered vein as shown in Figure 3D. Scale bar is 1 cm. (B) X-ray fluorescence (XRF) elemental maps of the Sr K-edge, Ca K-edge, Y K-edge, and U L-edge taken at X-ray fluorescence microprobe (XFM) beamline; area corresponding to the small orange rectangle in A. (C) XRF elemental maps of the Al K-edge, Y L-edge, Mg K-edge, S K-edge, and U M-edge taken at Tender Energy Spectroscopy (TES) beamline; area corresponding to the larger purple rectangle in A.

Downloaded from https://pubs.geoscienceworld.org/gsa/geosphere/article-pdf/15/6/1958/4880292/1958.pdf
by Michael D. Campbell

4.2.1 Fluorite

Fluorite is moderately to highly elevated in U, with concentrations of 15–1500 ppm (Data Set S2 [footnote 1]). Pb and Th concentrations are, in most cases, much lower than 1 ppm. Fluorite has a range of $^{238}U/^{206}Pb$ from 200 to 2024 and ages that range from 6.2 to 3.2 Ma (Fig. 12). The oldest fluorite identified is dark green, forms directly on the host rock (Fig. 2A), and gives an age of 6.2 ± 0.4 Ma (Fig. 12A). Slightly younger ages are found in the well-studied sample BRT-7 shown in Figures 2E, 5, 6, and 9; this sample has two geochemically different generations (Fig. 6). The older fluorite generation, found on the bottom of the sample as oriented in Figure 6, gives an age of 5.5 ± 1.1 Ma (Fig. 12B). The next oldest fluorite forms very thin coatings of dark-purple fluorite on clasts of host rock (Fig. 2B); it gives an age of 5.2 ± 0.1 Ma (Fig. 12C). A dark-green fluorite that follows purple nacrite and fluorite precipitation gives an age of 5.0 ± 0.5 Ma (Fig. 12D). Green fluorite clasts within calcite-cemented breccia (Figs. 2F and 2G) are the next youngest generation and give overlapping ages of 4.9 ± 0.3 Ma and 4.7 ± 0.2 Ma (Figs. 12E and 12F). All of the above ages are in fact indistinguishable from ca. 5 Ma. The second generation of fluorite found in the top of the BRT-7 (Figs. 2E, 5, 6, and 9) is 4.1 ± 0.6 Ma (Fig. 12G). A dark-green fluorite that follows green nacrite gives the youngest fluorite age at 3.2 ± 0.4 Ma (Fig. 12H).

4.2.2 Nacrite

Nacrite occurs in four different colors with variable U, Th, and Pb concentrations (Data Set S2 [footnote 1]). Th and Pb concentrations are far higher than fluorite, and thus the $^{238}U/^{206}Pb$ is generally lower. The ages of nacrite overlap with those of fluorite. The oldest generation of nacrite is tan and occurs as breccia clasts with host rock (Fig. 2C). This generation of nacrite is surrounded by a thin layer of purple fluorite and gives an indistinguishable age from that fluorite of 5.6 ± 1.3 Ma (Fig. 13A). A purple nacrite layer from the sample shown in Figure 2B clearly crosscuts the host rock and gives an age of 3.5 ± 1.9 Ma (Fig. 13B). Another purple nacrite layer capping green fluorite (Fig. 2D) and a pink nacrite (Fig. 2G) with surrounding green fluorite give indistinguishable ages of 3.4 ± 0.4 Ma and 3.3 ± 1.0 Ma (Figs. 13C and 13D). A green nacrite layer, also from Figure 2D, gives a slightly younger age of 3.3 ± 0.1 Ma (Fig. 13E). The youngest nacrite measured was a small green clast from the sample in Figure 2G, which gave an age of 2.8 ± 0.6 Ma (Fig. 13G).

4.2.3 Calcite

Calcite occurs as multiple generations with dissolution surfaces in between. For the most part, the calcite has low U and unfavorable $^{238}U/^{206}Pb$ (Data Set S2 [footnote 1]). A white calcite with curved crystals makes up the matrix material for most of the veins we studied and encases breccia clasts (Figs. 2F and 2G). This calcite has low U and low U-Pb and is therefore not suitable for dating; based on relative relationships, it occurs later than fluorite and the YHREE mineral. Another calcite sample has a distinctive brown color and has elevated Y and YHREE carbonates on its lower surface (Fig. 2H). The elevated Y, as well as the color and texture, suggest it is a separate generation from the breccia-cementing white calcite. This calcite has some layers of high U-Pb. Combined, the calcite gives an age of 1.7 ± 0.1 Ma (Fig. 13F).

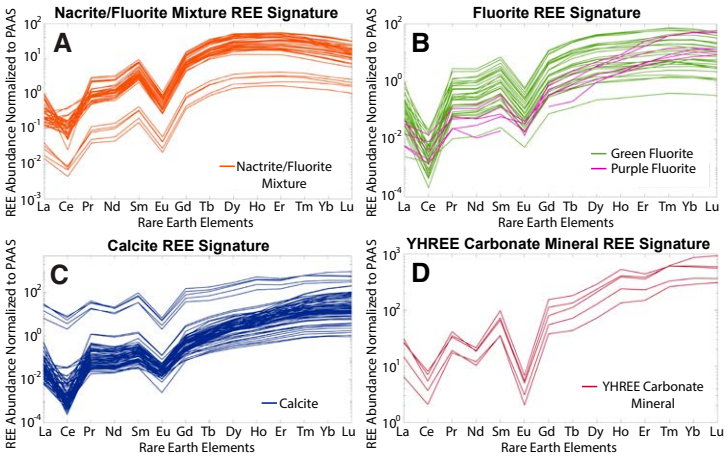

Figure 11. (A) Rare-earth element (REE) pattern for nacrite and fluorite mixture; (B) REE pattern for green and purple fluorite; (C) REE pattern for calcite; and (D) REE pattern for yttrium and heavy rare-earth element (YHREE) carbonate mineral.

5. DISCUSSION

5.1 U-Pb Geochronology

This study explores the utility of U-Pb dating of fluorite, nacrite, and calcite paragenesis in REE mineralization. Given the ubiquitous occurrence of these minerals in hydrothermal systems, U-Pb dating holds great potential for constraining the age of associated ore minerals. We use multiple microscopy techniques to investigate the relationships between fluorite, nacrite, and vein mineralization, and we combine these observations with LA-ICP-MS element mapping and U-Pb dating to provide absolute time constraints on REE mineralization.

An important contribution of this work is that fluorite and associated nacrite are far younger than the time of igneous crystallization and therefore must have been deposited by secondary fluid events. Rare-earth element ores are often assumed to be deposited during late stage igneous crystallization. However, the 6.2–2.8 Ma fluorite and nacrite ages strongly suggest that fluids responsible for mineralization are associated with Rio Grande rifting. Combining

Downloaded from https://pubs.geoscienceworld.org/gsa/geosphere/article-pdf/15/6/1958/4880292/1958.pdf
by Michael D. Campbell

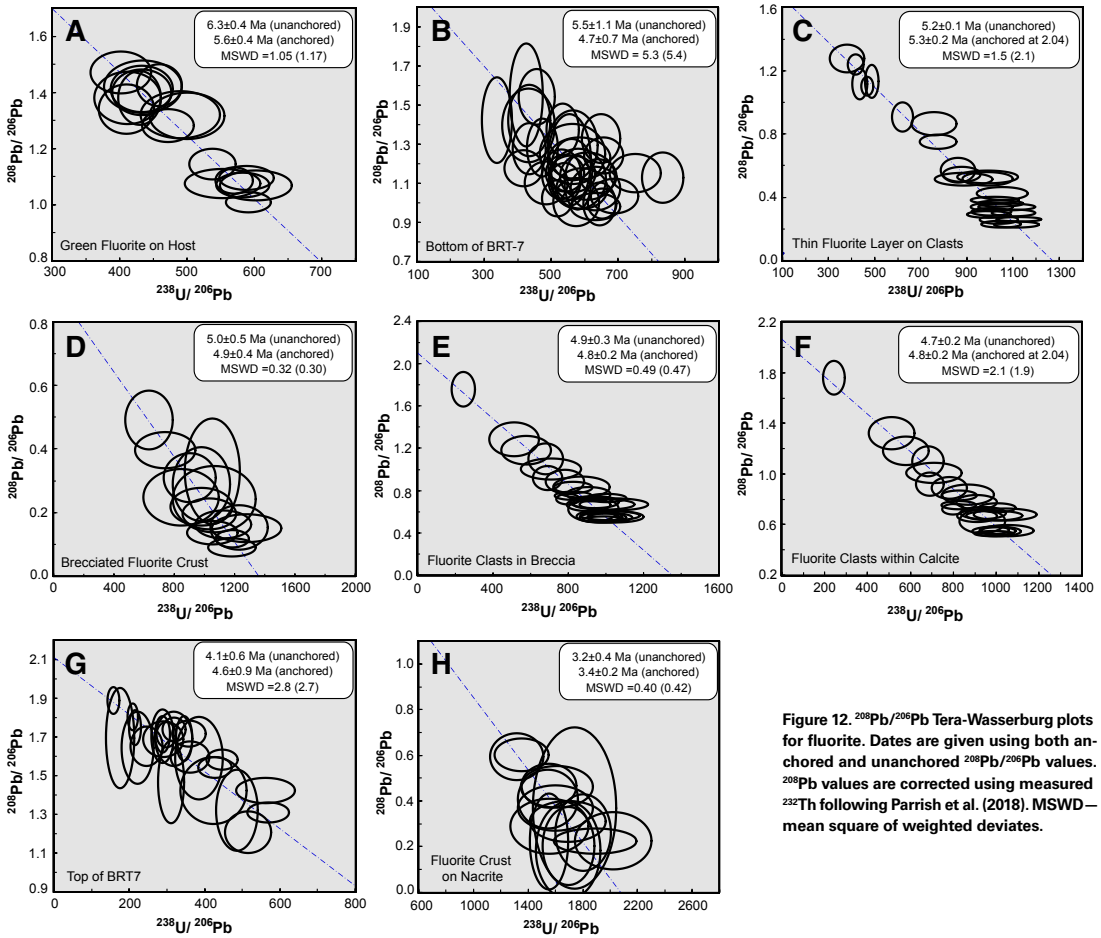

Figure 12. $^{208}Pb/^{206}Pb$ Tera-Wasserburg plots for fluorite. Dates are given using both anchored and unanchored $^{208}Pb/^{206}Pb$ values. ^{208}Pb values are corrected using measured ^{232}Th following Parrish et al. (2018). MSWD—mean square of weighted deviates.

geochronological evidence with the imaging techniques, we recognize the following sequence of events at Round Top: (1) fracturing and alteration of the host rock with deposition of fluorite on fracture surfaces; (2) further fracturing of host rock and early nacrite deposition, lined by a second generation of fluorite, in this case, both purple and green; (3) even younger nacrite and fluorite line veins within the fractures and are capped by green fluorite of the same ages; (4) brecciation of host and vein material with evidence of some dissolution of fluorite; (5) breccia clasts are lined by a YHREE carbonate; and (6) several generations of calcite, some of which are themselves lined by the YHREE carbonate (Fig. 14). The calcite that surrounds breccia clasts does not have U-Pb ratios that allow us to date it, but brown calcite found in association with it is 1.7 Ma (Fig. 2H). Nacrite has high REE, Th, and U, while fluorite has low REE with the same pattern, low Th, and high U. The white calcite that postdates the YHREE carbonate has extremely HREE-enriched patterns: up to 1000× HREE concentrations of post-Archean Australian shale (PAAS). The dated brown calcite has low REE concentrations, and no REE minerals are observed after its formation. Thus, REE mobility is constrained to be between 6.2 and 1.7 Ma.

5.2 Multiple Fluid Events over the Past 6.2 Ma

The fluid responsible for earliest fracture vein mineralization produced an intimate mixture of cryptocrystalline nacrite ($Al_2Si_2O_5(OH)_4$) and fluorite. The presence of nacrite may suggest hydrothermal activity, as it has been found

Downloaded from https://pubs.geoscienceworld.org/gsa/geosphere/article-pdf/15/6/1958/4880292/1958.pdf
by Michael D. Campbell

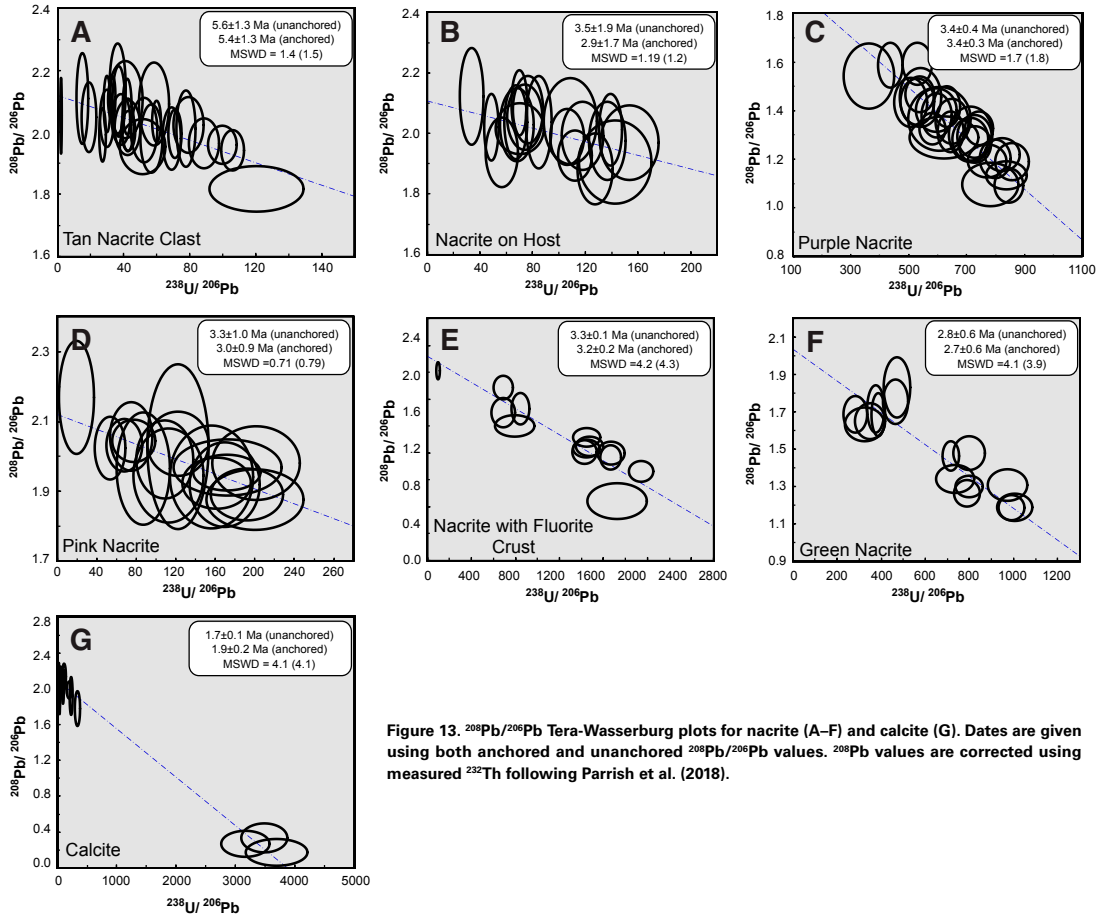

Figure 13. $^{208}Pb/^{206}Pb$ Tera-Wasserburg plots for nacrite (A–F) and calcite (G). Dates are given using both anchored and unanchored $^{208}Pb/^{206}Pb$ values. ^{208}Pb values are corrected using measured ^{232}Th following Parrish et al. (2018).

in association with hydrothermal fluorite in other areas (Polyakova, 1967). The presence of significant F in the fluid likely accounts for the solubility of Si and Al as well as the REE, U, and Th. As the fluid reached the fracture, changing conditions, such as seen with fault valves (Ramsay, 1980; Sibson, 1990) caused the precipitation of this nacrite/fluorite mix. The resulting deposit of nacrite/fluorite is enriched in U, Th, Y and REE suggesting that this fluid was a primary driver of trace element mobilization and enrichment. The close association between nacrite and fluorite suggests that this is a progression of precipitation from the same fluid event. U zoning within the fluorite suggests changing fluid conditions during mineral formation. REE patterns of nacrite and fluorite are similar to each other and show pronounced negative Ce and Eu anomalies, as well as enrichment of MREE-HREE relative to PAAS (or chondritic uniform reservoir [CHUR]) (Figs. 11A and 11B). The presence of a negative Ce anomaly is perhaps evidence that the fluid that deposited these minerals was highly oxidizing, which would have helped promote dissolution of primary minerals and trace-element mobilization. The negative Eu anomaly is similar to that measured by O'Neill et al. (2017) for the bulk Round Top rhyolite and is therefore not likely to be the result of fractionation in fluids related to vein mineralization. Fluorite has a range of ages from 6.2 to 3.2 Ma, with the earliest generation forming directly on the host rock. Later generations of fluorite clearly postdate nacrite and fluorite precipitation because these are always found capping the nacrite surface. The nacrite ranges in age from 5.6 to 2.8 Ma.

Brecciation of host rock, nacrite, and fluorite clearly demonstrates a later fluid event that likely accompanied fault movement. We find host rock and tan nacrite clasts lined by a purple fluorite that is 5.2 Ma. This fluorite has significantly greater HREE enrichment, relative to other REE, than any other

Downloaded from https://pubs.geoscienceworld.org/gsa/geosphere/article-pdf/15/6/1958/4880292/1958.pdf
by Michael D. Campbell

fluorite we analyzed (Fig. 11B) and occupies clast surfaces, similar to the mineralization of the YHREE mineral in later events. Fluorite and nacrite clasts ranging from 4.9 to 2.8 Ma are lined by an YHREE carbonate. A 4.1 Ma fluorite generation has resorption textures that demonstrate a fluid that was able to dissolve fluorite (Figs. 6, 9D, and 9E). It is not possible to say what caused the brecciation events, but many clasts have boundaries that clearly fit with neighboring clasts suggesting that some brecciation was in situ (Figs. 2B, 2C, and 2F). Importantly, these younger clasts are almost always lined by YHREE carbonate and are followed by white calcite with curved crystals. This calcite is depleted in LREE but is enriched HREE (Fig. 11C). We suggest that this YHREE mineral and calcite association is an evolution of precipitation from a fluid where the YHREE mineral is less soluble and precipitates first. The calcite growth could displace earlier minerals, but the brecciation must have occurred prior to the precipitation of the YHREE carbonate.

Clearly several distinct fluid events are recorded in Round Top veins. The fluorite and nacrite have a range of ages suggesting that a fluid with F was important from 6.2 to 2.8 Ma. Some of the fluorite has been brecciated and dissolved, demonstrating that a very different fluid chemistry followed fluorite mineralization. Finally, we see evidence for carbonate precipitation punctuated by multiple dissolution events that followed the brecciation events. Even with this complexity, two fluid types reasonably encompass the observations made: an early F-bearing fluid that resulted in multiple episodes of nacrite and fluorite precipitation, followed by one that dissolved fluorite and then precipitated carbonates presumably as it became saturated through mineral dissolution. However, what is less clear is the source of the REE. Rare-earth elements are highly enriched in nacrite and thus the first proposed fluid was able to mobilize REE. The REE patterns are enriched in the MREE and HREE with a pronounced positive hump across the MREEs (Fig. 11A). There are numerous REE-bearing minerals in the Round Top laccolith, and it is striking that one of the zircon generations shows abundant evidence for dissolution (Rubin et al., 1987; O'Neill et al., 2014, 2017). We hypothesize that the fluorine-bearing fluid was able to dissolve silicates and deliver the Al, Si, REE, and U to the veins. With the exception of the Ce anomaly, the REE pattern is similar to published patterns for zircons (O'Neill et al., 2017).

The second fluid can clearly dissolve fluorite as shown by resorption textures in vein fluorite. Given the oxidizing nature of this fluid, it is possible that it dissolved HREE-bearing yttrofluorite from the laccolith. Previous literature has suggested using sulfuric acid for dissolving yttrofluorite for extraction of REE (Pingitore et al., 2014; Negron et al., 2016). Within areas of the fluorite with evidence for dissolution, we see sulfur in close association with the YHREE carbonate (Fig. 9E). We speculate that the fluid was sulfuric acid bearing. A similar dissolution mechanism has been proposed in the Carlsbad area, where sulfuric acid is hypothesized to have been responsible for cavern formation in Permian carbonates (Davis, 1973; Jagnow, 1978; Davis, 1980; Hill, 1981).This sulfuric acid is thought to have resulted from Basin and Range uplift mobilizing oil and brines with associated H_2S that mixed with meteoric water as it neared the surface. Likewise, oxidation of sulfide minerals in wall rocks will also generate sulfuric acid. Regardless of the mechanism, uplift associated with Rio Grande rifting as well as Basin and Range faulting is important in the Trans-Pecos region and provides mechanisms for sulfuric acid formation.

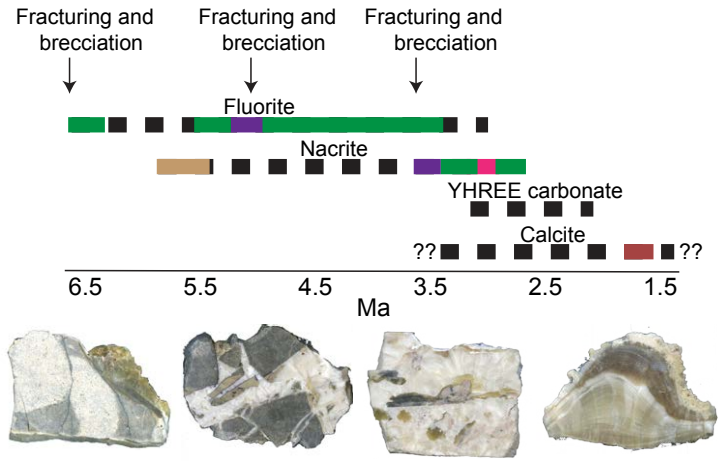

Figure 14. Paragenesis determined by the ages of fluorite, nacrite, and calcite. Each labeled line represents timing of crystallization of the specified mineral. Line colors represent mineralization color (i.e., purple = purple fluorite or purple nacrite crystallization). Dotted lines indicate undated (but possible) mineralization. Sample photos are representative of mineralization from 6.5 Ma to 1.5 Ma (going from left to right, decreasing in age). YHREE—yttrium heavy rare-earth element.

5.3 Round Top Vein Ages Match Period of Rio Grande Rift-Related Tectonism

To the north of Round Top, in the Bingham mine area of New Mexico, massive fluorite deposits in the Rio Grande rift have been attributed to a mantle source of fluorine (Partey et al., 2009). The ages for vein material at Round Top match the timing of a hiatus in Rio Grande rifting and a period of eastward tilting of the western Great Plains related to dynamic mantle upwelling (van Wijk et al., 2018). Across the Great Basin, there is a strong correlation between fluorine and transtensional tectonics (Holt et al., 2015, 2018). A recent synthesis of strain rates across the western United States demonstrates that the Rio Grande rift in the Trans Pecos region was under transtension between 12 and 4 Ma (Bahadori et al., 2018). The fluorite in the Bingham mine area has very low U and U-Pb and is not amenable to dating. Perhaps the difference at Round Top is that the fluid interacted with a U- and REE-enriched body. Based on the evolution of vein mineralization at Round Top, fluorine was important between 6.5 and 2.8 Ma, consistent with this being an interval of transtension in the Rio Grande rift. Magmatism of this age is not known in Trans-Pecos Texas (Henry and McDowell, 1986) and is limited and localized in the Rio Grande

Downloaded from https://pubs.geoscienceworld.org/gsa/geosphere/article-pdf/15/6/1958/4880292/1958.pdf
by Michael D. Campbell

rift in southern New Mexico (Aldrich et al., 1986). The results of radiometric dating of nacrite, fluorite, and calcite veins in this study suggest the potential to constrain episodes of transtensional tectonics and deep fluid input even in areas that lack contemporaneous magmatic bodies at the surface.

6. CONCLUSIONS

We show that there is great potential for LA-ICP-MS U-Pb dating of hydrothermal minerals to illuminate the timing of fluid events and to date associated ore deposits. At Round Top laccolith, we have evidence for multiple fluid events. Early fluid events have elevated REE with MREE-enriched patterns in nacrite and fluorite and range in age from 6.2 to 3.2 Ma. Later fluids brecciated and dissolved fluorite and nacrite and precipitated highly HREE-enriched carbonates: an YHREE carbonate followed by calcite. These minerals could not be directly dated but are bracketed by 2.8 Ma nacrite and a 1.7 Ma calcite that has low REE. The most important observation here is that the timing of mobilization greatly postdates igneous emplacement. Instead the timing is consistent with that of Rio Grande rifting. Fluorite deposits to the north in New Mexico are suggested to have a mantle source (Partey et al., 2009). Perhaps smaller amounts of fluorine fluxed through the Trans-Pecos area, mobilizing REE from various accessory minerals in the laccolith. It appears that an even more aggressive fluid followed that was capable of dissolving fluorides, the primary REE host in the laccolith, and brecciating the existing vein minerals and host rock. We speculate that this was a sulfuric acid–bearing fluid, perhaps due to mixing of H_2S-bearing brines with meteoric water, similar to that hypothesized for Carlsbad Caverns (Davis, 1973; Jagnow, 1978; Davis, 1980; Hill, 1981). A HREE carbonate and calcite were precipitated by this succeeding fluid. This fluid was followed by fluids that could both dissolve and precipitate calcite. A late generation of calcite with low REE but high U and U-Pb is dated at 1.7 Ma. We have not found evidence for REE mobilization that is later than this calcite generation.

This application of U-Pb dating of fluorite nacrite and elemental characterizing of a suite of vein minerals shows that this approach can be of use in future work understanding the geochemical processes that remobilize REE. More precise U-Pb geochronology on fluorite using LA-ICPMS could be of use in creating details chronologies of hydrothermal fluid events and ore mineralization.

ACKNOWLEDGMENTS, SAMPLES, AND DATA

We thank Perach Nuriel, Robert Holder, and editor Christopher Spencer for their constructive reviews and comments, which greatly improved the manuscript. The full data set beyond those published in this manuscript is available in Data Sets S1–S4, Supporting Information S1, and Table S1 (footnote 1). The authors declare no financial conflicts of interest. We thank Texas Mineral Resources Corporation for access to their Round Top property. Gavin Piccione was funded through a summer internship through Stony Brook University (SBU) Undergraduate Research and Creative Activities Program (URECA). Field work (Piccione, Rasbury, and Jaret) was partially supported through a SBU Department of Geosciences fund from Rich Parrish. Additional support for field work was provided by the III Yager Professorship of the Jackson School of Geosciences (Kyle) and the State of Texas Advanced Resource Recovery (STARR) program through the University of Texas at Austin, Bureau of Economic Geology, Mineral Resource Program (Elliott). Summer 2018 undergraduate interns Nattarika Saengkhueankaeo (Ford) and Kevin Hatton who were supported by GEOPREP (National Science Foundation grant) provided some of the laser ablation data and initial data reduction. We thank Timothy Glotch (Stony Brook) for access and use of the Raman microscope. Wendy Austin-Giddings did the initial laser ablation analyses of sample BRT7 at NERC Isotope Geochronology Laboratory. Daniel Davis and William Holt have been involved in numerous discussions of the tectonic context that has helped to bring this research together. Aaron Celestian was involved in discussion and interpretation of XRD data. Portions of this work were performed at beamlines X15B and X26A of the National Synchrotron Light Source (NSLS), Brookhaven National Laboratory. X26A was supported by the Department of Energy (DOE) Geosciences (DE-FG02-92ER14244 to The University of Chicago, Center for Advanced Radiation Sources [CARS]). Use of the NSLS was supported by DOE under contract no. DE-AC02-98CH10886. Portions of this research were also performed at the Tender Energy Spectroscopy (TES), X-ray fluorescence microprobe (XFM), and submicron-resolution X-ray spectroscopy (SRX) beamlines and used resources of the National Synchrotron Light Source II, a U.S. Department of Energy (DOE) Office of Science User Facility operated for the DOE Office of Science by Brookhaven National Laboratory under contract no. DE-SC0012704. Construction of and work at the TES beamline and initial measurements at X15B were partly funded by the National Science Foundation–Earth Sciences (EAR-1128957), National Aeronautics and Space Association (NNX13AD12G), and the Department of Energy, Geosciences (DE-FG02-12ER16342). This research also used resources of the Advanced Photon Source, a U.S. Department of Energy (DOE) Office of Science User Facility operated for the DOE Office of Science by Argonne National Laboratory under contract no. DE-AC02-06CH11357. We acknowledge the support of GeoSoilEnviroCARS (Sector 13), which is supported by the National Science Foundation–Earth Sciences (EAR-1128799) and the Department of Energy, Geosciences (DE-FG02-94ER14466). Partial funding came from the National Science Foundation grant number EAR-1814091.

REFERENCES CITED

Aldrich, M.J., Chapin, C.E., and Laughlin, A.W., 1986, Stress history and tectonic development of the Rio Grande Rift, New Mexico: Journal of Geophysical Research, v. 91, p. 6199–6211, https://doi.org/10.1029/JB091iB06p06199.

Bahadori, A., Holt, W.E., and Rasbury, E.T., 2018, Reconstruction modeling of crustal thickness and paleotopography of western North America since 36 Ma: Geosphere, v. 14, no. 3, p. 1207–1231, https://doi.org/10.1130/GES01604.1.

Barker, D.S., 1987, Tertiary alkaline magmatism in Trans-Pecos Texas Early, *in* Fitton, J.G., and Upton, B.G.J., eds., Alkaline Igneous Rocks: Geological Society of London Special Publication 30, p. 415–431.

Bau, M., 1991, Rare-earth element mobility during hydrothermal and metamorphic fluid-rock interaction and the significance of the oxidation state of europium: Chemical Geology, v. 93, p. 219–230, https://doi.org/10.1016/0009-2541(91)90115-8.

Bau, M., and Dulski, P., 1995, Comparative study of yttrium and rare-earth element behaviours in fluorine-rich hydrothermal fluids: Contributions to Mineralogy and Petrology, v. 119, no. 2–3, p. 213–223, https://doi.org/10.1007/BF00307282.

Bau, M., and Moller, P., 1992, Rare earth element fractionation in metamorphogenic hydrothermal calcite, magnesite and siderite: Mineralogy and Petrology, v. 45, p. 231–246, https://doi.org/10.1007/BF01163114.

Burisch, M., Walter, B.F., and Markl, G., 2017, Silicification of hydrothermal gangue minerals in Pb-Zn-Cu-fluorite-quartz-baryte veins: The Canadian Mineralogist, v. 55, no. 3, p. 501–514, https://doi.org/10.3749/canmin.1700005.

Cánovas, C.R., Macías, F., López, R.P., and Nieto, J.M., 2018, Mobility of rare earth elements, yttrium and scandium from a phosphogypsum stack: Environmental and economic implications: The Science of the Total Environment, v. 618, p. 847–857, https://doi.org/10.1016/j.scitotenv.2017.08.220.

Davis, D.G., 1973, Sulfur in Cottonwood Cave, Eddy County, New Mexico: Bulletin of the National Speleological Society, v. 35, no. 3, p. 89–95.

Davis, D.G., 1980, Cave development in the Guadalupe Mountains: A critical review of recent hypotheses: The NSS Bulletin, v. 42, no. 3, p. 42–48.

Debruyne, D., Hulsbosch, N., and Muchez, P., 2016, Unraveling rare earth element signatures in hydrothermal carbonate minerals using a source-sink system: Ore Geology Reviews, v. 72, p. 232–252, https://doi.org/10.1016/j.oregeorev.2015.07.022.

Downloaded from https://pubs.geoscienceworld.org/gsa/geosphere/article-pdf/15/6/1958/4880292/1958.pdf
by Michael D. Campbell

Elliott, B.A., 2018, Petrogenesis of heavy rare earth element enriched rhyolite: Source and magmatic evolution of the Round Top laccolith, Trans-Pecos, Texas: Basel, Switzerland, Minerals, v. 8, no. 10, p. 423, https://doi.org/10.3390/min8100423.

Fan, H., Xie, Y., Wang, K., Tao, K., and Wilde, S.A., 2004, REE daughter minerals trapped in fluid inclusions in the Giant Bayan Obo REE-Nb-Fe deposit, inner Mongolia, China: International Geology Review, v. 46, p. 638–645, https://doi.org/10.2747/0020-6814.46.7.638.

Genna, D., Gaboury, D., and Roy, G., 2014, Evolution of a volcanogenic hydrothermal system recorded by the behavior of LREE and Eu: Case study of the Key Tuffite at Bracemac-McLeod deposits, Matagami, Canada: Ore Geology Reviews, v. 63, p. 160–177, https://doi.org/10.1016/j.oregeorev.2014.04.019.

Gieré, R., 1990, Hydrothermal mobility of Ti, Zr and REE: Examples from the Bergell and Adamello contact aureoles (Italy): Terra Nova, v. 2, p. 60–67, https://doi.org/10.1111/j.1365-3121.1990.tb00037.x.

Henry, C.D., and McDowell, F.W., 1986, Geochronology of magmatism in the Tertiary volcanic field, Trans-Pecos Texas, *in* Price, J.G., Henry, C.D., Parker, D.F., and Barker, D.S., eds., Texas: Igneous Geology of Trans-Pecos Texas: Texas Bureau of Economic Geology, University of Texas at Austin, Guidebook 23, p. 99–122.

Henry, C.D., and Price, J.G., 1984, Variations in Caldera Development in the Tertiary Volcanic Field of Trans-Pecos Texas: Journal of Geophysical Research, v. 89, p. 8765–8786, https://doi.org/10.1029/JB089iB10p08765.

Henry, C.D., Price, J.G., and Miser, D.E., 1989, Geology and Tertiary igneous activity of the Hen Egg Mountain and Christmas Mountains Quadrangles, Big Bend region: Trans-Pecos, Texas: Bureau of Economic Geology, University of Texas at Austin, https://doi.org/10.23867/RI0183D.

Hill, C.A., 1981, Speleogenesis of Carlsbad Caverns and other caves in the Guadalupe Mountains: Bowling Green, Kentucky, Proceedings of the International Congress of Speleology, p. 143–144.

Holt, W.E., Rasbury, T., Wang, X., and Piccione, G.G., 2015, A measured correlation between fluorine concentrations in geothermal springs and Great Basin crustal strain rates: A new geochemical tracer for mantle fluid input: Geological Society of America Abstracts with Programs, v. 47, no. 7, p. 818.

Holt, W.E., Rasbury, T., Bahadori, A., Shen, W., and Kim, J., 2018, Fluorine concentrations in geothermal springs as an indicator of rheological weakening promoting active deformation in Western North America: American Geophysical Union abstract #T21G-0319.

Horstwood, M.S.A., Ko, J., Gehrels, G., Jackson, S.E., Mclean, N.M., Paton, C., and Schoene, B., 2016, Community-derived standards for LA-ICP-MS U-(Th-) Pb geochronology–uncertainty propagation, age interpretation and data reporting: Geostandards and Geoanalytical Research, v. 40, p. 311–332, https://doi.org/10.1111/j.1751-908X.2016.00379.x.

Jagnow, D.H., 1978, Geology and speleogenesis of Ogle Cave, New Mexico: Bulletin of the National Speleological Society, v. 40, no. 1, p. 7–18.

Lanzirotti, A., Tappero, R., and Schulze, D.G., 2010, Practical application of synchrotron-based hard X-ray microprobes in soil sciences, *in* Singh, B., and Grafe, M., eds., Synchrotron-Based Techniques in Soils and Sediments: Developments in Soil Science, v. 34: Elsevier, p. 27–72, https://doi.org/10.1016/S0166-2481(10)34002-5.

Li, Xian-hua, Liu, D., Sun, M., Li, W., Liang, X.-R., and Liu, Y., 2004, Precise Sm-Nd and U-Pb isotopic dating of the supergiant Shizhuyuan polymetallic deposit and its host granite, SE China: Geological Magazine, v. 141, p. 225–231, https://doi.org/10.1017/S0016756803008823.

Li, Xiaochun, and Zhou, M., 2015, Multiple stages of hydrothermal REE remobilization recorded in fluorapatite in the Paleoproterozoic Yinachang Fe-Cu-(REE) deposit, Southwest China: Geochimica et Cosmochimica Acta, v. 166, p. 53–73, https://doi.org/10.1016/j.gca.2015.06.008.

Lottermoser, B.G., 1992, Rare earth elements and hydrothermal ore formation processes: Ore Geology Reviews, v. 7, no. 1, p. 25–41, https://doi.org/10.1016/0169-1368(92)90017-F.

Ludwig, K.R., 1998, On the treatment of concordant uranium-lead ages: Geochimica et Cosmochimica Acta, v. 62, no. 4, p. 665–676, https://doi.org/10.1016/S0016-7037(98)00059-3.

Ludwig, K.R., 2003, User's manual for a geochronological toolkit for Microsoft Excel (Isoplot/Ex version 3.0): Berkeley Geochronology Center Special Publication No. 4.

Ludwig, K.R., 2012, User's Manual for Isoplot 3.75: A Geochronological Toolkit for Microsoft Excel: Berkeley Geochronology Center Special Publication No. 5.

Muehlberger, W.R., 1980, Texas lineament revisited, *in* Trans-Pecos region, southeastern New Mexico and west Texas: New Mexico Geological Society Fall Field Conference Guidebook, v. 31, p. 113–121.

Negron, L., Pingitore, N., and Gorski, D., 2016, Porosity and permeability of Round Top Mountain rhyolite (Texas, USA) favor coarse crush size for rare earth element heap leach: Minerals, v. 6, p. 16, https://doi.org/10.3390/min6010016.

Ngwenya, T.B., 1994, Hydrothermal rare earth mineralisation in carbonatites of the Tundulu complex, Malawi: Processes at the fluid/rock interface: Geochimica et Cosmochimica Acta, v. 58, no. 9, p. 2061–2072, https://doi.org/10.1016/0016-7037(94)90285-2.

Northrup, P., 2019, The TES beamline (8-BM) at NSLS-II : Tender-energy spatially resolved X-ray absorption spectroscopy and X-ray fluorescence imaging: Journal of Synchrotron Radiation, v. 26, https://doi.org/10.1107/S1600577519012761.

Northrup, P., Leri, A., and Tappero, R., 2016, Applications of "tender" energy (1-5 keV) X-ray absorption spectroscopy in life sciences: Protein and Peptide Letters, v. 23, p., http://doi.org/10.2174/0929866523666160107114505.

O'Neill, L.C., Kyle, J.R., and Elliott, B., 2014, REE-Be-U-F Enriched Mineralization of the Round Top Laccolith, Sierra Blanca Peaks, Trans-Pecos Texas [Master's thesis]: Austin, Texas, The University of Texas at Austin.

O'Neill, L.C., Elliott, B.A., and Kyle, J.R., 2017, Mineralogy and crystallization history of a highly differentiated REE-enriched hypabyssal rhyolite: Round Top laccolith, Trans-Pecos, Texas: Mineralogy and Petrology, v. 111, no. 4, p. 569–592, https://doi.org/10.1007/s00710-017-0511-5.

Parrish, R.R., Parrish, C.M., and Lasalle, S., 2018, Vein calcite dating reveals Pyrenean orogen as cause of Paleogene deformation in southern England: Journal of the Geological Society, v. 175, https://doi.org/10.1144/jgs2017-107.

Partey, F., Lev, S., Casey, R., Widom, E., Lueth, V.W., and Rakovan, J., 2009, Source of fluorine and petrogenesis of the Rio Grande Rift-type barite-fluorite-galena deposits: Economic Geology and the Bulletin of the Society of Economic Geologists, v. 104, p. 505–520, https://doi.org/10.2113/gsecongeo.104.4.505.

Paton, C., Hellstrom, J., Paul, B., Woodhead, J., and Hergt, J., 2011, Iolite: Freeware for the visualisation and processing of mass spectrometric data: Journal of Analytical Atomic Spectrometry, v. 26, p. 2508–2518, https://doi.org/10.1039/c1ja10172b.

Pfaff, K., Romer, R.L., and Markl, G., 2009, U-Pb ages of ferberite, chalcedony, agate, 'U-mica' and pitchblende: Constraints on the mineralization history of the Schwarzwald ore district: European Journal of Mineralogy, v. 21, no. 4, p. 817–836, https://doi.org/10.1127/0935-1221/2009/0021-1944.

Pingitore, N., Clague, J., and Gorski, D., 2014, Round Top Mountain rhyolite (Texas, USA), a massive, unique Y-bearing-fluorite-hosted heavy rare earth element (HREE) deposit: Journal of Rare Earths, v. 32, no. 1, p. 90–96, https://doi.org/10.1016/S1002-0721(14)60037-5.

Polyakova, O.P., 1967, Nacrite from the fluorite deposits of Eastern Transbaykalia: International Geology Review, v. 9, p. 225–229, https://doi.org/10.1080/00206816709474459.

Ponnurangam, A., Bau, M., Brenner, M., and Koschinsky, A., 2015, Mussel shells of Mytilus edulis as bioarchives of the rare earth elements and yttrium distribution in seawater and the potential impact of pH and temperature on the partitioning behaviour: Biogeosciences Discussions, v. 12, no. 17, p. 14911–14939, https://doi.org/10.5194/bgd-12-14911-2015.

Price, J.G., Henry, C.D., Barker, D.S., and Parker, D.F., 1987, Alkalic rocks of contrasting tectonic settings in Trans-Pecos Texas, *in* Morris, E.M., and Pasteris, J.D., eds., Mantle Metasomatism and Alkaline Magmatism: Geological Society of America Special Paper 215, p. 335–346, https://doi.org/10.1130/SPE215-p335.

Price, J.G., Rubin, J.N., Henry, C.D., Pinkston, T.L., Tweed, S.W., and Koppenaal, D.W., 1990, Rare-metal enriched peraluminous rhyolites in a continental arc, Sierra Blanca area, Trans-Pecos Texas; Chemical modification by vapor-phase crystallization, *in* Stein, H.J., and Hannah, J.L., eds., Ore-Bearing Granite Systems; Pedogenesis and Mineralizing Processes: Geological Society of America Special Paper 246, p. 103–120 https://doi.org/10.1130/SPE246-p103.

Ramsay, J.G., 1980, The crack-seal mechanism of rock deformation: Nature, v. 284, p. 135–139, https://doi.org/10.1038/284135a0.

Ricketts, J.W., Kelley, S.A., Karlstrom, K.E., Schmandt, B., and Donahue, M.S., 2016, Synchronous opening of the Rio Grande rift along its entire length at 25–10 Ma supported by apatite (U-Th)/He and fission-track thermochronology, and evaluation of possible driving mechanisms: Geological Society of America Bulletin, v. 128, no. 3/4, p. 397–424, https://doi.org/10.1130/B31223.1.

Roberts, N.M.W., Rasbury, E.T., Parrish, R.R., Horstwood, M.S.A., Condon, D.J., and Smith, C.J., 2017, A calcite reference material for LA-ICP-MS U-Pb geochronology: Geochemistry, Geophysics, Geosystems, v. 18, p. 2807–2814, https://doi.org/10.1002/2016GC006784.

Rowe, M.C., Lassiter, J.C., and Goff, K., 2015, Basalt volatile fluctuations during continental rifting: An example from the Rio Grande Rift, USA: Geochemistry, Geophysics, Geosystems, v. 16, p. 1254–1273, https://doi.org/10.1002/2014GC005649.

Rubin, J.N., Price, J.G., Henry, C.D., and Koppenaal, D.W., 1987, Cryolite-bearing and rare metal-enriched rhyolite, Sierra Blanca Peaks, Hudspeth County, Texas: The American Mineralogist, v. 72, no. 11–12, p. 1122–1130.

Downloaded from https://pubs.geoscienceworld.org/gsa/geosphere/article-pdf/15/6/1958/4880292/1958.pdf
by Michael D. Campbell

Rubin, J.N., Henry, C.D., and Price, J.G., 1993, The mobility of zirconium and other "immobile" elements during hydrothermal alteration: Chemical Geology, v. 110, p. 29–47, https://doi.org/10.1016/0009-2541(93)90246-F.

Shannon, W.M., 1986, Lithogeochemical characterization of intrusive rocks comprising the Quitman-Sierra Blanca igneous complex, Hudspeth County, Texas [M.S. thesis]: University of Texas at El Paso, https://digitalcommons.utep.edu/dissertations/AAIEP02340.

Shannon, W.M., and Goodell, P.C., 1986, Lithogeochemistry of intrusive rocks of the Quitman-Sierra Blanca igneous complex, Hudspeth County, *in* Price, J.G., Henry, C.D., Parker, D.F., and Barker, D.S., eds., Texas: Igneous Geology of Trans-Pecos Texas: Texas Bureau of Economic Geology, University of Texas at Austin, Guidebook 23, p. 225–226.

Sheard, E.R., Williams-Jones, A.E., Heiligmann, M., Pederson, C., and Trueman, D.L., 2012, Controls on the concentration of zirconium, niobium, and the rare earth elements in the Thor Lake Rare Metal Deposit, Northwest Territories, Canada: Economic Geology and the Bulletin of the Society of Economic Geologists, v. 107, no. 1, p. 81–104, https://doi.org/10.2113/econgeo.107.1.81.

Sibson, R.H., 1990, Conditions for fault-valve behaviour, *in* Knipe, R.J., and Rutter E.H., eds., Deformation Mechanisms, Rheology and Tectonics: Geological Society of London Special Publication 54, p. 15–28, https://doi.org/10.1144/GSL.SP.1990.054.01.02.

Tan, S., Zhou, J., Li, B., and Zhao, J., 2017, In situ Pb and bulk Sr isotope analysis of the Yinchanggou Pb-Zn deposit in Sichuan Province (SW China): Constraints on the origin and evolution of hydrothermal fluids: Ore Geology Reviews, v. 91, p. 432–443, https://doi.org/10.1016/j.oregeorev.2017.09.012.

van Dongen, M., Weinberg, R.F., and Tomkins, A.G., 2010, REE-Y, Ti, and P remobilization in magmatic rocks by hydrothermal alteration during Cu-Au deposit formation: Economic Geology and the Bulletin of the Society of Economic Geologists, v. 105, no. 4, p. 763–776, https://doi.org/10.2113/gsecongeo.105.4.763.

van Wijk, J., Koning, D., Axen, G., Coblentz, D., Gragg, E., and Sion, B., 2018, Tectonic subsidence, geoid analysis, and the Miocene–Pliocene unconformity in the Rio Grande rift, southwestern United States: Implications for mantle upwelling as a driving force for rift opening: Geosphere, v. 14, p. 684–709, https://doi.org/10.1130/GES01522.1.

Walter, B.F., Gerdes, A., Kleinhanns, I.C., Von Eynatten, H., Kreissl, S., and Markl, G., 2018, The connection between hydrothermal fluids, mineralization, tectonics and magmatism in a continental rift setting: Fluorite Sm-Nd and hematite and carbonates U-Pb geochronology from the Rhinegraben in SW Germany: Geochimica et Cosmochimica Acta, v. 240, p. 11–42, https://doi.org/10.1016/j.gca.2018.08.012.

Williams-Jones, A.E., Migdisov, A.A., and Samson, I.M., 2012, Hydrothermal mobilisation of the rare earth elements—A tale of "Ceria" and "Yttria": Elements, v. 8, no. 5, p. 355–360, https://doi.org/10.2113/gselements.8.5.355.

Yang, F., Wang, G., Cao, H., Li, R., Tang, L., Huang, Y., Zhang, H., Xue, F., Jia, W., and Guo, N., 2017, Geoscience frontiers timing of formation of the Hongdonggou Pb-Zn polymetallic ore deposit, Henan Province, China: Evidence from Rb-Sr isotopic dating of sphalerites: Geoscience Frontiers, v. 8, no. 3, p. 605–616, https://doi.org/10.1016/j.gsf.2016.06.001.

Downloaded from https://pubs.geoscienceworld.org/gsa/geosphere/article-pdf/15/6/1958/4880292/1958.pdf
by Michael D. Campbell